



Numerical modeling of composite solids using an immersed meshfree Galerkin method

C.T. Wu^{a,*}, Y. Guo^a, E. Askari^b

^a Livermore Software Technology Corporation, Livermore, CA 94551, USA

^b The Boeing Company, Seattle, WA 98124, USA

ARTICLE INFO

Article history:

Received 6 May 2012

Received in revised form 9 July 2012

Accepted 10 September 2012

Available online 28 September 2012

Keywords:

A. Particle-reinforcement

A. Immersed structure

B. Interface

C. Meshfree method

C. Convex approximation

ABSTRACT

A novel meshfree approach for the elastic analysis of composite solids is proposed. This approach introduces a new meshfree discretization technique that can be applied to the composite solids with overlapping sub-domains. Since each sub-domain is discretized individually by the finite element model, substantial user interaction for generating the conforming mesh is avoided. A meshfree convex approximation is employed taking advantage of the naturally conforming property to approximate the overlapping sub-domains and to enforce the global Dirichlet boundary condition. In addition, a Kronecker-delta property is imposed on the approximation of interfacial nodes leading to a point-wise continuity in displacements across the interface. As a result, a non-conforming meshfree Galerkin method for the elasticity interface problem is devised and is shown to satisfy an optimal error estimate in the energy norm. This method is applicable to both macro and microscopic analyses of composite solids such as particle and fiber-reinforced composites. Three numerical benchmarks in two-dimensional case are provided to demonstrate effectiveness and accuracy of the proposed method.

© 2012 Elsevier Ltd. All rights reserved.

1. Introduction

The elasticity of composite solids such as particle and fiber-reinforced composites is a boundary value problem (BVP) that can be modeled by the elliptic equations containing discontinuous coefficients [1]. The discontinuous coefficients in BVPs introduce jump conditions across the interface in displacements as well as in flux. These jump conditions generally are determined by the relevant physics. The elasticity interface problems of composite solids presented in this paper consider the homogenous jump conditions which arise in a wide range of mathematical modeling in material science and bio-medical applications such as the elastic analysis of rubber compounds [2,3], modeling of bone structures [4] and simulation of brain shifting [5]. The conventional finite element method (FEM) in this context is to generate a matching (conforming) mesh across the material interface and use standard finite element shape functions to approximate solutions of the BVPs. As a result, each element basically contains only one material and the element basis functions are independent of the jump conditions. However, generating 2D and 3D matching meshes suitable for the finite element analysis is difficult in cases where interfaces are present in

irregular geometries. Construction of matching meshes in interface problem generally requires substantial user interaction and is time-consuming. Therefore from user's point of view, it is advantageous to use discretization that is not matching at the material interfaces for the composite solids analysis.

A flexible way to couple mismatching meshes across the interface is to use the mortar finite element method [6]. It is a domain decomposition technique that enforces the jump conditions across the interface by Lagrange multipliers and results in a saddle point problem which requires appropriate solvers. Unfortunately, arbitrary choice of approximation space for Lagrange multipliers may violate the inf-sup condition [7,8] and can lead to instabilities that eventually cause artificial oscillations in the traction fields. A different variational approach for the discretization of interface problem is offered by Nitsche's method [9]. Such discretization incorporates interface conditions approximately, but consistently, by penalizing the jump of the primal variable (displacement) and avoids the use of Lagrange multipliers. Consequently, the resulting linear system is positive definite and does not suffer from ill-conditioning. The Nitsche's method has a close relationship [10] with Barbosa and Hughes' least-squares stabilized Lagrange multiplier formulation [11] in circumventing the inf-sup condition. Despite its non-trivial implementation and a need to determine the penalty parameters, Nitsche's method has been shown to preserve optimal convergence in L^2 and energy norms for elasticity interface problems [12].

* Corresponding author. Address: Livermore Software Technology Corporation (LSTC), 7374 Las Positas Road, Livermore, CA 94551, USA. Tel.: +1 925 245 4529; fax: +1 925 449 2507.

E-mail address: ctwu@lstc.com (C.T. Wu).

Alternatively, the partition of unity method (PUM) [13,14] employs a priori knowledge of the solution at interfaces to obtain special finite element spaces. Later in [15], the method was referred to as generalized finite element method (GFEM), since the classical FEM is a special case of this method [16]. The ability to choose a wide variety of enrichment functions in GFEM allows it to approximate non-smooth solutions of BVPs on domains having internal boundaries, corners or multiple cracks [2,17]. The enrichment function is extrinsic to the finite element basis function, thereby introducing new degrees of freedom. In other words, the enrichment function can, in principle, be arbitrary and are certainly not limited to polynomials. This advantage, however, is achieved at a high computational cost due to expensive numerical integration [16]. The extended finite element method (XFEM) [18] is an application of PUM for problems of interface tracking and crack growth. XFEM enriches the standard finite element shape functions with additional continuous enrichment function (Ramp function) or discontinuous enrichment function (Heaviside function or Step function) to approximate the solution near the interface. The enrichment function exists only at the nodes of the elements that intersect the interface. This allows XFEM to accommodate elements that do not conform to the interface. Solution spaces of XFEM using discontinuous enrichment function do not generally satisfy the Dirichlet jump condition on the interface. As the one in the mortar finite element method, linear or tied constraint methods such as Lagrangian multipliers, penalty methods and bubble-stabilized method [19] are often utilized to enforce the Dirichlet jump condition. While such methods provide high fidelity predictions of the structure response in composites, their robustness has not yet been demonstrated on large-scale simulations of composite solids [20] such as heterogeneous microstructures. The calculations in XFEM involving small inclusions require the generation of small elements thus very time consuming. Even with high quality adaptive meshes, the nodal enrichment procedure in single element containing multiple interfaces is a significant challenge in particular for the three-dimensional problem.

Both GFEM and XFEM treat the material interface implicitly using the concept of level set method. Similar implicit boundary representation techniques have been developed based on a uniform Cartesian mesh under different versions of embedded or fictitious domain approaches. Among them are finite cell method for geometrical modeling of embedded problems [21], immersed finite element method for fluid-structure interaction problems [22] and immersed finite element method for elasticity interface problems [23,24]. The recently developed immersed finite element method (IFEM) [23] is also rooted in the GFEM. In IFEM, the finite element basis functions are constructed to satisfy the homogenous jump conditions across the material interface whereas the mesh itself can be independent of the interface. Since the homogenous jump conditions are only satisfied point-wise at the intersections of interface and element edge, the finite element basis functions defined in this way could be discontinuous across edges of interface elements [25] and thus non-conforming. A sophisticated conforming local basis functions has been introduced to non-conforming IFEM by enlarging the support of some standard basis functions in the non-conforming finite element space such that the continuity condition in displacements can be enforced. The conforming linear IFEM [25] was shown to be optimally convergent in L^2 and energy norms. Despite its improved accuracy, conforming IFEM is far more complex than non-conforming IFEM and the extension to three-dimensional case is not clear.

In comparison to finite element method, meshfree method is known to provide a higher accuracy in solid analysis in particular for the large deformation problems. The analysis of elasticity interface problem in composite solids is a new area in recent meshfree developments [26–28]. Cordes and Moran [29] impose the jump

condition by adding an interface constraint in the variational formulation and solve the equation by Lagrange multiplier method. Since the material interface serves as a visibility criterion for the construction of meshfree approximation in the composite solid model, a set of interface nodes has to be manually added along the interface together with properly adjusted integration cells for the domain integration. A parallel research [30,31] is devoted to the development of a particular meshfree approximation that contains discontinuities in the derivatives across the material interface. This approach requires defining the interface nodes in the numerical model and may not be easily performed when the interface involves complex geometry or three-dimensional object. The introduction of discontinuities to meshfree approximation has also recently been applied to the immersed particle method [32] to model the fluid-structure interaction problem. A special jump functions was also incorporated with meshfree approximation by enforcing its consistency conditions [33] and therefore additional unknowns are not needed. Recently, a discontinuous Galerkin meshfree formulation was proposed by Wang et al. [34] based on an incompatible patch-based meshfree approximation to model the material interface in composite solid. Since the continuities of displacement and normal flux are imposed weakly at the variational level, this formulation also does not acquire additional degrees of freedom.

On the other hand, conventional meshfree approximation requires special considerations to impose the boundary conditions. Wu and Koishi [3] proposed a convex generalized meshfree approximation to simplify the treatment of boundary conditions in meshfree method and applied to the micromechanical analysis of particle-reinforced rubber. The employment of convex generalized meshfree approximation to the solid analysis was shown to be less sensitive to the nodal support size [35]. The convex generalized meshfree approximation was also shown to be more robust than the non-convex meshfree approximation such as moving least-squares (MLSs) [36] or reproducing kernel (RK) [37] approximations when low-order Gaussian quadrature rule is used for numerical integration. Park et al. [38] embarked on a detailed eigenanalysis for meshfree convex approximation and reported that a large critical time step can be used in the explicit dynamic analysis. Their dispersion analysis results also reveal that meshfree convex approximation exhibits smaller lagging phase and amplitude errors than conventional MLS approximation in the full-discretization of the wave equation. Other convex meshfree approximations [39,40] based on Shannon's entropy concept [41] and maximum entropy [42] principle were also developed and used to solve the incompressible problem [43] as well as the structural problem [44]. The convex generalized meshfree approximation was recently introduced [45] to the standard finite element method to solve the volumetric locking problems that present in the low-order displacement-based Galerkin method. More recently, this new technique was employed to the micromechanical analysis of three-dimensional particle-reinforced rubber composite in automotive tire applications [46]. Despite its success in resolving the volumetric locking problem, the new method inevitably depends on a conforming mesh in modeling the composite solid for the micromechanical analysis. Modeling material interface in composite solid using existing meshfree techniques still relies on a mesh generation of base material and inclusions for the domain integration. The generation of non-overlapping meshes for composite solids in particular for the fiber and particular reinforced composites remains challenging in both finite element and meshfree methods.

The aim of this paper is to present an alternative approach for elasticity of composite solid problem using meshfree method. A significant feature of our approach is its flexibility to adopt the overlapping meshes in composite solid that can be easily discretized using the finite element model. Therefore the discretized domain for the base material does not need to conform to the material interface.

As a consequence, there is no need to insert the interface nodes and their corresponding integration cells in the proposed method. All information regarding the geometry of material interface is stored in the geometrical model of inclusions, and solid mesh generation for inclusions can be as detail as possible to better represent the geometry of material interface. The mesh density of the inclusions can be independent of that in the base material in which a structured mesh can be easily generated for the base material. The resulting immersed meshfree method is attractive in the large-scale micro-mechanical modeling of composites since the periodic nodes along the boundary can be easily imposed through the structured mesh. In conforming FEM, additional efforts such as manual correction of mesh topology or employment of Fast Fourier Transformation method [20] have to be made to overcome the difficulty of constructing large meshes with homologous nodes at the periodic boundary. The proposed method is also particularly convenient in the material processing contexts when the morphology design is subjected to a change. The remainder of the paper is outlined as follows: In the next section, we define the elliptic boundary-value problem containing discontinuous coefficients and formulate the weak form of the equilibrium equation. In Section 3, we modify the variational formulation for the meshfree method to be used in the composite solid problem. The details of numerical discretization, approximation and domain integration for the modified variational method are described. A priori estimate is derived for the error measures in the energy norm. In Section 4, the numerical procedures of the immersed meshfree method are described. The discrete equations using the convex generalized meshfree approximation are presented in the same section. In Section 5, three two-dimensional numerical examples are studied. Final remarks are drawn in Section 6.

2. Problem description and variational equation

We consider an elastic solid occupying a bounded and open domain $\Omega \subset \mathbb{R}^2$ with Lipschitz boundary. Let $\partial\Omega_D$ and $\partial\Omega_N$ be two open subsets of boundary $\partial\Omega$ such that $\partial\Omega = \partial\Omega_D \cup \partial\Omega_N$ and $\partial\Omega_D \cap \partial\Omega_N = \emptyset$. $\mathbf{g}(\mathbf{x})$ is the prescribed displacement applied on the Dirichlet boundary $\partial\Omega_D$, and $\mathbf{t}(\mathbf{x}) \in L^2(\partial\Omega_N)$ is the prescribed traction applied on the Neumann boundary $\partial\Omega_N$ with \mathbf{n}_0 denoting the outward unit normal to the boundary $\partial\Omega_N$. The elastic body is composed of two perfectly bounded materials with zero-thickness interface Γ . The equilibrium configuration of the elastic body is characterized by the continuity of displacement and continuity of normal stress across the material interface Γ . The elasticity interface problem can be described by the following second-order elliptic boundary value problem with the associated homogenous Dirichlet and Neumann jump conditions on the interface Γ

$$\begin{cases} -\nabla \cdot (\mathbf{C}(\mathbf{x}) \cdot \nabla_s \mathbf{u}(\mathbf{x})) = \mathbf{f}(\mathbf{x}) & \mathbf{x} \in \Omega \setminus \Gamma \\ \mathbf{u} = \mathbf{g}(\mathbf{x}) & \mathbf{x} \in \partial\Omega_D \\ \mathbf{C}(\mathbf{x}) \cdot \nabla_s \mathbf{u}(\mathbf{x}) \cdot \mathbf{n}_0 = \mathbf{t}(\mathbf{x}) & \mathbf{x} \in \partial\Omega_N \\ [\mathbf{u}] = \mathbf{0} & \mathbf{x} \in \Gamma \\ [[\mathbf{C}(\mathbf{x}) \cdot \nabla_s \mathbf{u}(\mathbf{x}) \cdot \mathbf{n}]] = \mathbf{0} & \mathbf{x} \in \Gamma \end{cases} \quad (1)$$

where function $\mathbf{u}: \Omega \rightarrow \mathbb{R}^2$ is the displacement and $\mathbf{f}: \Omega \rightarrow \mathbb{R}^2$ is the prescribed body force over the domain Ω . Normally, $\mathbf{f} \in L^2(\Omega)$. The notation $\nabla_s \mathbf{u}$ denotes the symmetric gradient of the displacement, $\nabla_s \mathbf{u} = \frac{1}{2}(\nabla \mathbf{u} + (\nabla \mathbf{u})^T)$. Without loss of generality, we assume the interface Γ is a smooth and closed curve that divides the global domain Ω into two regions: Ω^+ representing the base material and Ω^- denoting the immersed media or inclusion such that their union gives the global domain Ω , $\bar{\Omega} = \bar{\Omega}^+ \cup \bar{\Omega}^-$ and $\Gamma = \partial\Omega^+ \cap \partial\Omega^-$ as depicted in Fig. 1. The symbol \mathbf{n} in Fig. 1 denotes the outward unit normal vector on Γ . For simplicity, we further assume a convex domain $\Omega^- \subset \mathbb{R}^2$ for inclusion. Correspondingly, we have a domain Ω^+ of base material which is non-convex. We also define the jump operator $[[\cdot]]$ by

$$[[\mathbf{q}]](\mathbf{x}) = \mathbf{q}^+(\mathbf{x}) - \mathbf{q}^-(\mathbf{x}) \quad (2)$$

in which $+$ and $-$ denote the two sides of the interface Γ with the jump of quantity q across the interface. The body force and material constants can exhibit discontinuities across the interface Γ , but have smooth restrictions $\mathbf{f}^+, \mathbf{C}^+$ to Ω^+ and $\mathbf{f}^-, \mathbf{C}^-$ to Ω^- . They are given by

$$\mathbf{f} = \begin{cases} \mathbf{f}^+ & \text{in } \Omega^+ \\ \mathbf{f}^- & \text{in } \Omega^- \end{cases} \quad \text{and} \quad \mathbf{C} = \begin{cases} \mathbf{C}^+ & \text{in } \Omega^+ \\ \mathbf{C}^- & \text{in } \Omega^- \end{cases} \quad (3)$$

The infinitesimal strain tensor $\boldsymbol{\varepsilon}(\mathbf{u})$ is defined by

$$\boldsymbol{\varepsilon}(\mathbf{u}) = \nabla_s \mathbf{u} = \frac{1}{2}(\nabla \mathbf{u} + (\nabla \mathbf{u})^T) \quad (4)$$

\mathbf{C}^+ and $\mathbf{C}^- \in L^\infty(\Omega)$ are elasticity tensors with major and minor symmetries and are corresponding to different materials in Ω^+ and Ω^- respectively. In the case of linear isotropic elasticity, we take \mathbf{C}^+ and \mathbf{C}^- to be constants. The Cauchy stress tensor $\boldsymbol{\sigma}$ and strain tensor $\boldsymbol{\varepsilon}$ have the following relationship

$$\begin{cases} \boldsymbol{\sigma}^+ = \mathbf{C}^+ \cdot \boldsymbol{\varepsilon} = 2\mu^+ \boldsymbol{\varepsilon} + \lambda^+ \text{tr}(\boldsymbol{\varepsilon}) \mathbf{I} & \text{in } \Omega^+ \\ \boldsymbol{\sigma}^- = \mathbf{C}^- \cdot \boldsymbol{\varepsilon} = 2\mu^- \boldsymbol{\varepsilon} + \lambda^- \text{tr}(\boldsymbol{\varepsilon}) \mathbf{I} & \text{in } \Omega^- \end{cases} \quad (5)$$

where the positive constants μ^+, μ^- and λ^+, λ^- are Lamé constants. The Lamé constants are related to the Young's modulus E and Poisson ratio ν by

$$\mu = \frac{E}{2(1+\nu)}, \quad \lambda = \frac{\nu E}{(1+\nu)(1-2\nu)} \quad (6)$$

The variational form of this problem is to find the displacement $\mathbf{u} \in \mathbf{V}^{\text{el}} = \{\mathbf{v} \in \mathbf{H}^1(\Omega); \mathbf{v} = \mathbf{g} \text{ on } \partial\Omega_D\}$ such that for all $\mathbf{v} \in \mathbf{V}$

$$a(\mathbf{u}, \mathbf{v}) = l(\mathbf{v}) \quad (7)$$

where the functional space $\mathbf{V} = \mathbf{H}_0^1(\Omega)$ consists of functions in Sobolev space $\mathbf{H}^1(\Omega)$ which vanish on the boundary $\partial\Omega$ and is defined by

$$\mathbf{V}(\Omega) = \{\mathbf{v} : \mathbf{v} \in \mathbf{H}^1, \mathbf{v} = \mathbf{0} \text{ on } \partial\Omega_D\} \quad (8)$$

The bilinear form $a(\cdot, \cdot)$ and linear functional $l(\cdot)$ are obtained by multiplying the test function $\mathbf{v} \in \mathbf{V}$ to both sides of Eq. (7) and integrating over the regions Ω^+ and Ω^- separately using Green's formula.

$$\begin{aligned} & \int_{\Omega^+} \mathbf{f}^+(\mathbf{x}) \cdot \mathbf{v} d\Omega + \int_{\Omega^-} \mathbf{f}^-(\mathbf{x}) \cdot \mathbf{v} d\Omega \\ &= - \int_{\Omega^+} \nabla \cdot (\mathbf{C}^+(\mathbf{x}) \cdot \nabla_s \mathbf{u}(\mathbf{x})) \cdot \mathbf{v} d\Omega - \int_{\Omega^-} \nabla \cdot (\mathbf{C}^-(\mathbf{x}) \cdot \nabla_s \mathbf{u}(\mathbf{x})) \cdot \mathbf{v} d\Omega \\ &= \int_{\Omega^+} \boldsymbol{\varepsilon}(\mathbf{u}) \cdot \mathbf{C}^+ \cdot \boldsymbol{\varepsilon}(\mathbf{v}) d\Omega - \int_{\Gamma} \mathbf{C}^+(\mathbf{x}) \cdot \nabla_s \mathbf{u}(\mathbf{x}) \cdot \mathbf{n}^+ \cdot \mathbf{v} d\Gamma \\ &+ \int_{\Omega^-} \boldsymbol{\varepsilon}(\mathbf{u}) \cdot \mathbf{C}^- \cdot \boldsymbol{\varepsilon}(\mathbf{v}) d\Omega - \int_{\Gamma} \mathbf{C}^-(\mathbf{x}) \cdot \nabla_s \mathbf{u}(\mathbf{x}) \cdot \mathbf{n}^- \cdot \mathbf{v} d\Gamma \\ &- \int_{\partial\Omega_N} (\mathbf{t} \cdot \mathbf{v}) d\partial\Omega \end{aligned} \quad (9)$$

Using the fact that $\mathbf{n}^+ = -\mathbf{n}^-$, we can rewrite the above equation to

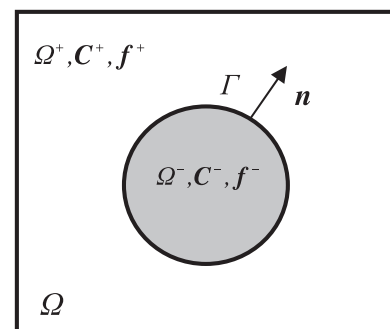


Fig. 1. Graphical depiction for interface elasticity problem.

$$\begin{aligned} & \int_{\Omega^+} \mathbf{f}^+(\mathbf{x}) \cdot \mathbf{v} d\Omega + \int_{\Omega^-} \mathbf{f}^-(\mathbf{x}) \cdot \mathbf{v} d\Omega = \int_{\Omega^+} \boldsymbol{\varepsilon}(\mathbf{u}) \cdot \mathbf{C}^+ \cdot \boldsymbol{\varepsilon}(\mathbf{v}) d\Omega \\ & + \int_{\Omega^-} \boldsymbol{\varepsilon}(\mathbf{u}) \cdot \mathbf{C}^- \cdot \boldsymbol{\varepsilon}(\mathbf{v}) d\Omega - \int_{\partial\Omega_N} (\mathbf{t} \cdot \mathbf{v}) d\partial\Omega \\ & - \int_{\Gamma} [\mathbf{C}(\mathbf{x}) \cdot \nabla_s \mathbf{u}(\mathbf{x}) \cdot \mathbf{n}] \cdot \mathbf{v} d\Gamma \end{aligned} \quad (10)$$

Applying the homogenous Neumann jump condition to Eq. (10) yields

$$\begin{aligned} & \int_{\Omega^+} \boldsymbol{\varepsilon}(\mathbf{u}) \cdot \mathbf{C}^+ \cdot \boldsymbol{\varepsilon}(\mathbf{v}) d\Omega + \int_{\Omega^-} \boldsymbol{\varepsilon}(\mathbf{u}) \cdot \mathbf{C}^- \cdot \boldsymbol{\varepsilon}(\mathbf{v}) d\Omega - \int_{\Omega^+} \mathbf{f}^+ \cdot \mathbf{v} d\Omega \\ & - \int_{\Omega^-} \mathbf{f}^- \cdot \mathbf{v} d\Omega - \int_{\partial\Omega_N} \mathbf{t} \cdot \mathbf{v} d\partial\Omega = a(\mathbf{u}, \mathbf{v}) - l(\mathbf{v}) = 0 \end{aligned} \quad (11)$$

where

$$a(\mathbf{u}, \mathbf{v}) = \int_{\Omega^+} \boldsymbol{\varepsilon}(\mathbf{u}) \cdot \mathbf{C}^+ \cdot \boldsymbol{\varepsilon}(\mathbf{v}) d\Omega + \int_{\Omega^-} \boldsymbol{\varepsilon}(\mathbf{u}) \cdot \mathbf{C}^- \cdot \boldsymbol{\varepsilon}(\mathbf{v}) d\Omega \quad (12)$$

$$l(\mathbf{v}) = \int_{\Omega^+} \mathbf{f}^+ \cdot \mathbf{v} d\Omega + \int_{\Omega^-} \mathbf{f}^- \cdot \mathbf{v} d\Omega + \int_{\partial\Omega_N} \mathbf{t} \cdot \mathbf{v} d\partial\Omega \quad (13)$$

It is noted that the elasticity tensors \mathbf{C}^+ and \mathbf{C}^- are symmetric, and homogenous Neumann jump condition is enforced in the variational level. Obviously, the bilinear form $a(\cdot, \cdot)$ in Eq. (12) is symmetric, bounded and coercive by Friedrichs inequality. The existence and uniqueness of the problem is ensured by the Lax–Milgram theorem [1].

3. Immersed meshfree method for composite solids

This section first focuses on the development of a new meshfree discretization that spans across the material interface. The definition of computation domain for the proposed method and the construction of the meshfree approximation that satisfies a point-wise continuity across the interface are subsequently described. Finally, a primal problem which is equivalent to a degenerated Lagrangian-type mortar method is devised and followed by a proof of the optimality.

3.1. Immersed meshfree discretization and integration cells

For simplicity, we assume that Ω is a convex polygonal domain and only consider the case of pure displacement problem under homogenous boundary condition ($\partial\Omega_D = 0$). The standard meshfree Galerkin method is formulated on a finite dimensional space $\mathbf{V}_h \subset \mathbf{V}$ employing the variational formulation of Eq. (11) to find $\mathbf{u}_h \in \mathbf{V}_h$ such that

$$a(\mathbf{u}_h, \mathbf{v}_h) = l(\mathbf{v}_h) \forall \mathbf{v}_h \in \mathbf{V}_h \quad (14)$$

where $\mathbf{V}_h = \text{span}\{\Psi_I; I \in Z_I\}$ and Z_I is an index set. $\{\Psi_I(\mathbf{x})\}_{I \in Z_I}$ are shape functions constructed using meshfree convex approximation [35] and will be described later in this section. We also let $r_I \subset \Omega$ be the interior of the supp $\Psi_I(\mathbf{x})$. We assume that r_I is star-shaped with respect to a ball $b_I \subset r_I$ and there exists a constant $C_r > 0$ such that [47]

$$\frac{\text{diam}(r_I)}{\text{diam}(b_I)} \geq C_r, \forall I \in Z_I \quad (15)$$

We let $h_I = \text{diam}(r_I)$ denote the nodal support radius and assume the following overlapping condition [35]

$$\exists M \in \mathbb{R} \quad \forall \mathbf{x} \in \Omega \quad \text{card } Z_I \leq M \quad (16)$$

Often, a shape function $\Psi_I(\mathbf{x})$ is associated with a particle $\mathbf{x}_I \in R^2$ and particles are distinct. Using the superposition principle for the above linear system, the discrete bilinear form in Eq. (14) can be re-expressed by

$$\begin{aligned} a(\mathbf{u}_h, \mathbf{v}_h) &= \int_{\Omega^+} \boldsymbol{\varepsilon}(\mathbf{u}_h) \cdot \mathbf{C}^+ \cdot \boldsymbol{\varepsilon}(\mathbf{v}_h) d\Omega + \int_{\Omega^-} \boldsymbol{\varepsilon}(\mathbf{u}_h) \cdot \mathbf{C}^- \cdot \boldsymbol{\varepsilon}(\mathbf{v}_h) d\Omega \\ &= \int_{\Omega^+ \cup \Omega^-} \boldsymbol{\varepsilon}(\mathbf{u}_h) \cdot \mathbf{C}^+ \cdot \boldsymbol{\varepsilon}(\mathbf{v}_h) d\Omega + \int_{\Omega^-} \boldsymbol{\varepsilon}(\mathbf{u}_h) \cdot \mathbf{C}^- \cdot \boldsymbol{\varepsilon}(\mathbf{v}_h) d\Omega \\ &\quad - \int_{\Omega^-} \boldsymbol{\varepsilon}(\mathbf{u}_h) \cdot \mathbf{C}^+ \cdot \boldsymbol{\varepsilon}(\mathbf{v}_h) d\Omega = \int_{\Omega^+ \cup \Omega^-} \boldsymbol{\varepsilon}(\mathbf{u}_h) \cdot \mathbf{C}^+ \cdot \boldsymbol{\varepsilon}(\mathbf{v}_h) d\Omega \\ &\quad + \int_{\Omega^-} \boldsymbol{\varepsilon}(\mathbf{u}_h) \cdot (\mathbf{C}^- - \mathbf{C}^+) \cdot \boldsymbol{\varepsilon}(\mathbf{v}_h) d\Omega \end{aligned} \quad (17)$$

Similarly, we have the discrete linear functional to be rewritten as

$$\begin{aligned} l(\mathbf{v}_h) &= \int_{\Omega^+} \mathbf{f}^+ \cdot \mathbf{v}_h d\Omega + \int_{\Omega^-} \mathbf{f}^- \cdot \mathbf{v}_h d\Omega \\ &= \int_{\Omega^+ \cup \Omega^-} \mathbf{f}^+ \cdot \mathbf{v}_h d\Omega + \int_{\Omega^-} \mathbf{f}^- \cdot \mathbf{v}_h d\Omega - \int_{\Omega^-} \mathbf{f}^+ \cdot \mathbf{v}_h d\Omega \\ &= \int_{\Omega^+ \cup \Omega^-} \mathbf{f}^+ \cdot \mathbf{v}_h d\Omega + \int_{\Omega^-} (\mathbf{f}^- - \mathbf{f}^+) \cdot \mathbf{v}_h d\Omega \end{aligned} \quad (18)$$

The expression of discrete forms in Eqs. (17) and (18) allows us to reset the meshfree computation domain by two overlapping sub-regions; namely $\Omega^+ \cup \Omega^-$ and Ω^- . The advantage of overlapping sub-regions is their flexibility to accommodate complex immersed structures in which mismatching discretizations can be made easily and independently in each sub-region using finite element model. Since the computation domain Ω^- is “immersed” in computation domain $\Omega^+ \cup \Omega^-$ under the meshfree Galerkin framework, we refer this method as an immersed meshfree Galerkin method. Fig. 2 is an illustration of overlapping sub-regions which shows a convex inclusion immersing in a base matrix using two overlapping finite element meshes. It is evident that for the single-phase system ($\mathbf{C}^+ = \mathbf{C}^-$ and $\mathbf{f}^+ = \mathbf{f}^-$) the modified variational formulation can be degenerated to the standard meshfree Galerkin formulation.

Consequently, we can define the computational sub-regions as follows:

Given a bounded domain $\Omega \subset R^2$, we consider sub-regions Ω_1 and Ω_2 to be the overlapping sub-regions satisfying

$$\Omega = \cup_{i=1}^2 \Omega_i \quad (19)$$

where $\Omega_1 = \Omega^+ \cup \Omega^-$ is the computation domain containing the composite solid. In other words, the computation domain Ω_1 of composite solid is composed of sub-region Ω^+ for base material and inclusion $\Omega_2 = \Omega^-$ for inclusion. We assume that each Ω_i is partitioned by a finite element triangulation T_{h_i} which can be completely independent of the other. Typically, interface-fitted nodes are generated by the partition in sub-region Ω_2 . For simplicity, we further assume that none of the nodes generated in two sub-regions coincide. In the case where two nodes collide in sub-region Ω_2 , they are merged to keep the procedure in the construction of meshfree approximation well-defined.

In the sub-region Ω_1 , the total number of meshfree nodes consists of a set of component nodes that overlap and cover the domain Ω . Fig. 3a shows the overlapping nodes of Fig. 2. The overlapping nodes include a set of structured nodes from sub-region Ω_1 and a set of interface-fitted nodes and interior nodes from sub-region Ω_2 . Fig. 3b is the associated finite element mesh in the partitioning of sub-region Ω_1 . The finite element mesh in Fig. 3b also serves as the integration cells needed for meshfree domain integration in sub-region Ω_1 that appears in the first term on RHS of Eqs. (17) and (18). Let $Z_I = \{\mathbf{x}_I, I = 1, \dots, NP\}$ be the set of distinct nodes in Ω_1 , NP indicates the total number of overlapping nodes in sub-region Ω_1 . For each $\mathbf{x}_I \in Z_I$, $\Psi_I(\mathbf{x})$ denotes the corresponding meshfree shape function. We define the meshfree interpolant of $\mathbf{u}(\mathbf{x})$ by the formula

$$\mathbf{u}^I(\mathbf{x}) = \sum_{I=1}^{NP} \Psi_I(\mathbf{x}) \mathbf{u}(\mathbf{x}_I) = \sum_{I=1}^{NP} \Psi_I(\mathbf{x}) \mathbf{u}_I \quad \forall \mathbf{x} \in \Omega_1 \quad (20)$$

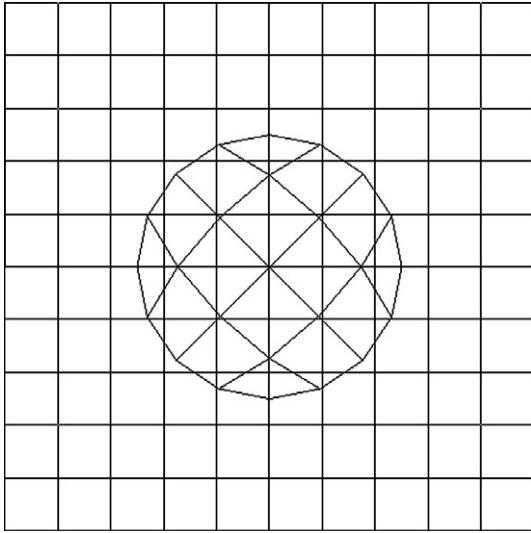


Fig. 2. Creating overlapping discretizations in the immersed structure by two finite element meshes.

where $\mathbf{u}_I = \mathbf{u}(\mathbf{x}_I)$ is called the ‘generalized’ displacement of node I . In other words, $\mathbf{u}^I(\mathbf{x})$ is considered as an interpolant of $\mathbf{u}(\mathbf{x})$ in a generalized sense. In general, conventional meshfree approximations are not interpolants, i.e., $\mathbf{u}_I \neq \mathbf{u}^I(\mathbf{x}_I)$. For this reason, special treatment [48] is required to impose the essential boundary conditions on the global boundary $\partial\Omega$ of the model problem. In this study an alternative meshfree approximation that restores a weak Kronecker-delta property at the boundary, the convex meshfree approximation [39,40], is utilized to allow the direct treatment of essential boundary conditions on $\partial\Omega$ for elasticity interface problem. We employ the generalized meshfree approximation method (GMF) [3,35] to obtain the meshfree convex approximation. The first-order convex GMF approximation is constructed using the inverse tangent basis function and the cubic spline window function is chosen to be the weight function in GMF method. Giving a convex hull $\mathbf{co}(Z_I)$ of a node set $Z_I = \{\mathbf{x}_I, I = 1, \dots, NP\} \subset R^2$ defined by

$$\mathbf{co}(Z_I) = \left\{ \sum_{I=1}^{NP} \alpha_I \mathbf{x}_I \mid \alpha_I \in R, \sum_{I=1}^{NP} \alpha_I = 1, \alpha_I \geq 0, \mathbf{x}_I \in Z_I, 1 \leq I \leq NP \right\} \quad (21)$$

the GME method is to construct a convex approximation of a given (smooth) function \mathbf{u} in the form of Eq. (20) such that the shape function $\Psi_I: \mathbf{co}(Z_I) \rightarrow R$ satisfies the following linear polynomial reproduction property

$$\sum_{I=1}^{NP} \Psi_I(\mathbf{x}) \mathbf{x}_I = \mathbf{x} \quad \forall \mathbf{x} \in \mathbf{co}(Z_I) \quad (22)$$

The detailed derivation of GMF method and the corresponding mathematical properties can be found in [35].

The convex approximation space constructed by GMF method is a subspace of $H_0^1(\Omega)$ and conforms to the boundary conditions if the approximating domain is convex. Ideally this conforming meshfree approximation secures H^1 -compatibility and the homogeneous Dirichlet jump condition across the interface is verified automatically. On the other hand, the meshfree approximation also introduces the non-locality [49] across the interface. This gives rise to a solution that exhibits a smearing near the interface. To remove the smearing, we invoke a second meshfree approximation in sub-region Ω_2 , e.g. by zero extension in the sub-region Ω_1 .

To be more precise, we let $\tilde{Z}_2 = \{\tilde{\mathbf{x}}_l, l = 1, \dots, MP\} \subset Z_1$ be the subset nodes that contain the overlapping nodes in the sub-region Ω_2 . MP is the total number of overlapping nodes in sub-region Ω_2 . Fig. 4a shows the overlapping nodes in sub-region Ω_2 . We also define $\tilde{Z}_2 = \{\tilde{\mathbf{x}}_l, l = 1, \dots, IP\} \subset \tilde{Z}_1 \subset Z_1$ to be the subset nodes that collect the interface-fitted nodes along the boundary of sub-region Ω_2 . IP is the total number of interface-fitted nodes. Fig. 4b is the associated finite element mesh of sub-region Ω_2 as well as the integration cells for meshfree domain integration that is needed in assembly of the second term on RHS of Eqs. (17) and (18). Analogously, every function $\tilde{\mathbf{u}}_h(\mathbf{x}) \in \tilde{V}_{h2}(\Omega_2)$ has a unique representation of the form

$$\tilde{\mathbf{u}}_h(\mathbf{x}) = \sum_{I=1}^{MP} \tilde{\Psi}_I(\mathbf{x}) \tilde{\mathbf{u}}_I \quad \forall \mathbf{x} \in \Omega_2 \quad (23)$$

Since the sub-region Ω_2 is assumed to be convex, the subspace $\tilde{V}_{h2}(\Omega_2)$ is defined by

$$\tilde{V}_{h2}(\Omega_2) = \{ \mathbf{v} : \mathbf{v}|_{\Omega_2} \in H^1(\Omega_2), \mathbf{v} = \mathbf{0} \text{ on } \partial\Omega \cup \partial\Omega_2 \} \quad (24)$$

Apparently, the subspace $\tilde{V}_{h2}(\Omega_2)$ is not a subset of subspace $V_h(\Omega_1)$, i.e., $\tilde{V}_{h2}(\Omega_2) \not\subset V_h(\Omega_1)$. Since the approximations in sub-region Ω_1 and sub-region Ω_2 are constructed independently, the meshfree shape functions $\tilde{\Psi}_I(\mathbf{x})$ and $\Psi_I(\mathbf{x})$ of the same node $\mathbf{x}_I \in \tilde{Z}_2 \subset Z_1$ are not necessarily the same. This is true in particular when support of node \mathbf{x}_I covers the interface Γ , i.e.,

$$\tilde{\Psi}_I(\mathbf{x}) \neq \Psi_I(\mathbf{x}) \text{ for } \mathbf{x}_I \in \tilde{Z}_2 \subset Z_1 \text{ and } \text{supp}(\mathbf{x}_I) \cap \Gamma \neq \emptyset \quad (25)$$

The support of shape function in sub-region Ω_2 is defined by

$$\text{supp}(\mathbf{x}_I) = \text{supp}(\tilde{\Psi}_I(\mathbf{x})) = \{ \mathbf{x} \mid \mathbf{x} \in \Omega_2 \text{ and } \tilde{\Psi}_I(\mathbf{x}) \neq 0 \} \quad (26)$$

As a result, it leads to a non-conforming meshfree approximation and the continuity of displacement across the interface is not

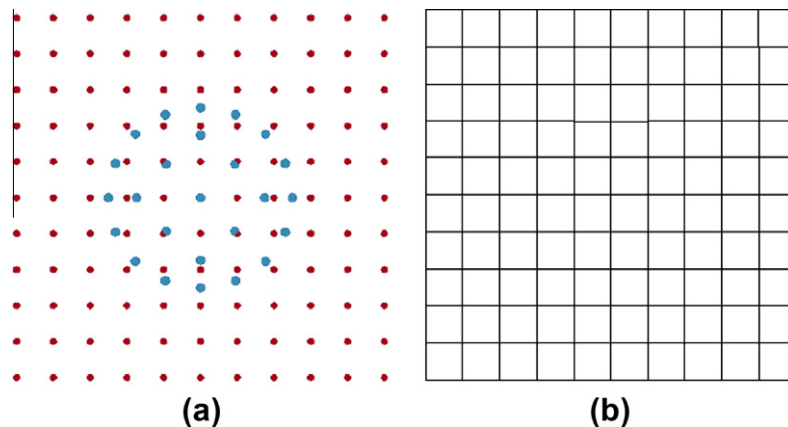


Fig. 3. Computation domain of base matrix. (a) Meshfree discretization. (b) Integration cells.

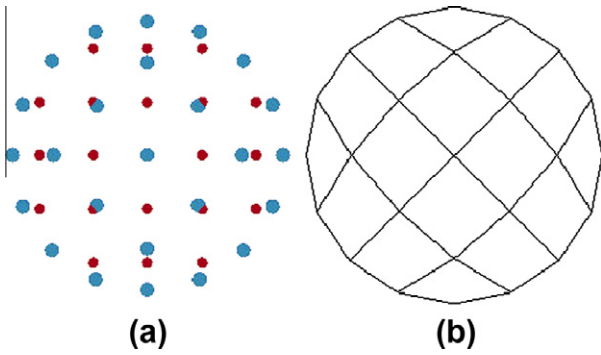


Fig. 4. Computation domain of inclusion. (a) Meshfree discretization. (b) Integration cells.

ensured. A one-dimensional example is shown in Fig. 5 to illustrate the non-conforming meshfree approximation using the immersed meshfree method. Because the homogenous Dirichlet jump condition is not satisfied at the interface, a procedure like the mortar technique for the coupling of two different triangulations is needed to achieve an optimal approximation.

3.2. Construction of meshfree approximation and modified variational formulation

In mortar finite element method, the non-conforming problem is caused by the non-matching meshes across the interface where no sharing nodes are established to provide the displacement continuity. Therefore, an additional constraint equation corresponding to the Dirichlet jump condition is required to connect the disjointed nodes between two triangulations. In standard mortar finite element method [6], the constraint equation is imposed weakly across the interface and is sufficient to guarantee an approximation with a consistency error of order h if the weak solution \mathbf{u} is smooth enough. However in immersed meshfree method, the sharing nodes are well-defined in the subset of interface-fitted nodes $\tilde{\tilde{Z}}_2 = \{\tilde{\tilde{x}}_l, l = 1, \dots, IP\}$. Indeed, the non-conformity of approximation in immersed meshfree method is due to the non-matching meshfree shape functions in the overlapping domain as illustrated in Fig. 5. Since the sub-region Ω_2 is immersed in the sub-region $\Omega_1(\Omega_2 \subset \Omega_1)$, we can redefine the approximation in sub-region Ω_1 such that $\tilde{\mathbf{V}}_{h2}(\Omega_2) \subset V_h(\Omega_1)$ and $\tilde{\Psi}_l(\mathbf{x}) = \Psi_l(\mathbf{x})$ for $\mathbf{x}_l \in \tilde{\tilde{Z}}_2 \subset Z_1$.

This can be achieved by decomposing the approximation in sub-region Ω_1 into two approximations in non-overlapping sub-domains ($\Omega_1 \setminus \Omega_2$ and Ω_2) and enforcing the nodal-wise continuity in displacement by introducing the Kronecker-delta property to the interface-fitted nodes set $\tilde{\tilde{Z}}_2$. Namely we define a new constrained discrete meshfree approximation space by

$$\hat{\mathbf{V}}_h(\Omega) = \prod_{i=1}^2 \tilde{\mathbf{V}}_{hi}(\Omega_i) \tag{27}$$

where the definition of subspace $\tilde{\mathbf{V}}_{h2}(\Omega_2) \subset \hat{\mathbf{V}}_h(\Omega)$ is given in Eq. (24) and additional subspace $\tilde{\mathbf{V}}_{h1}(\Omega_1)$ is defined by

$$\tilde{\mathbf{V}}_{h1}(\Omega_1) = \{\mathbf{v} : \mathbf{v}|_{\Omega_1 \setminus \Omega_2} \in \mathbf{H}^1(\Omega_1 \setminus \Omega_2), \mathbf{v} = \mathbf{0} \text{ on } \partial\Omega\} \subset \hat{\mathbf{V}}_h(\Omega) \tag{28}$$

We note that $\tilde{\mathbf{V}}_{hi}(\Omega_i), i = 1, 2$ stand for the spaces of linear conforming meshfree approximations that satisfy homogenous Dirichlet boundary conditions on $\partial\Omega \cap \partial\Omega_i, i = 1, 2$ in the sub-regions $\Omega_1 \setminus \Omega_2$ and Ω_2 respectively. Let $\tilde{\tilde{Z}}_1 = \{\tilde{\tilde{x}}_l, l = 1, \dots, LP\} \subset Z_1$ be the subset nodes such that

$$\tilde{\tilde{Z}}_1 = (Z_1 \setminus \tilde{\tilde{Z}}_2) \cup \tilde{\tilde{Z}}_2 \text{ and } LP = NP - MP + IP \tag{29}$$

In a one dimensional case, the new approximation is conforming since $\tilde{\mathbf{V}}_h(\Omega) \subset \mathbf{V}(\Omega)$. An improved meshfree approximation of Fig. 5 is shown in Fig. 6. Since the shape function of the interface-fitted node possesses the Kronecker-delta property, the continuity is imposed across the interface.

However, this is not the case in a two dimensional problem. Since sub-region $\Omega_1 \setminus \Omega_2$ is not convex (by assuming Ω_2 is convex previously), the approximation of the interface-fitted nodes generated by the GMF method does not possess a Kronecker-delta property. In other words, the displacement continuity at the interface-fitted node does not hold. A graphic sketch of this non-conforming approximation near the interface is given in Fig. 7.

In the general case, it is difficult to construct a conforming approximation across the interface. We will look into the possibility of constructing a conforming meshfree approximation for the interface problem in the future. In this study, we consider to impose the displacement continuity weakly and point-wisely across the interface by introducing the Kronecker-delta property to the approximation of the interface-fitted nodes. This can be done by either employing a singular kernel function [3,50,51] to the interface-fitted nodes or applying a transformation method [48,50] to those nodes whose supports cover the interface nodes. We have adopted the transformation method in this study. With the introduction of Kronecker-delta property to the shape functions at the

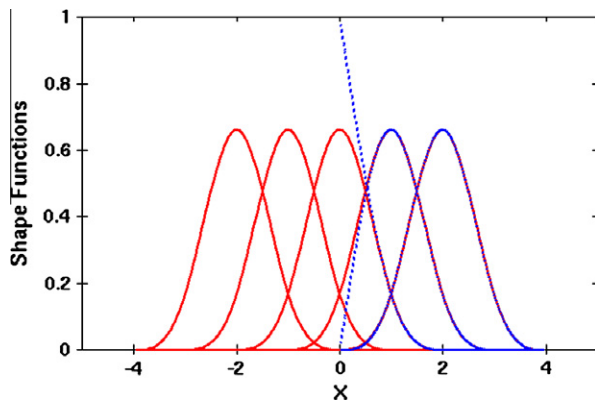


Fig. 5. Non-conforming meshfree approximation near the interface $x=0$: shape functions in sub-region Ω_1 are denoted by solid red lines and shape functions in sub-region Ω_2 are denoted by dash blue lines. (For interpretation of the references to colour in this figure legend, the reader is referred to the web version of this article.)

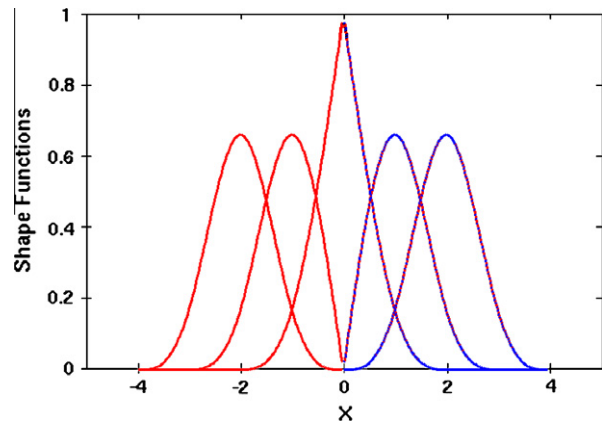


Fig. 6. Conforming meshfree approximation near the interface $x=0$: shape functions in sub-region Ω_1 are denoted by solid red lines and shape functions in sub-region Ω_2 are denoted by dash blue lines. (For interpretation of the references to colour in this figure legend, the reader is referred to the web version of this article.)

interface-fitted nodes set $\tilde{Z}_2 = \{\tilde{\mathbf{x}}_l, l = 1, \dots, lP\}$, the reconstructed meshfree shape functions in sub-region Ω_1 have the following form:

$$\Omega_1 : \begin{cases} \hat{\Psi}_l^1(\mathbf{x}) & \text{if } \mathbf{x}_l \in \tilde{Z}_1, \mathbf{x} \in \Omega_1 \setminus \Omega_2 \\ \hat{\Psi}_l^2(\mathbf{x}) = \tilde{\Psi}_l(\mathbf{x}) & \text{if } \mathbf{x}_l \in \tilde{Z}_2, \mathbf{x} \in \Omega_2 \\ \hat{\Psi}_l^1(\mathbf{x}_j) = \hat{\Psi}_l^2(\mathbf{x}_j) = \delta_{lj} & \text{if } \mathbf{x}_l, \mathbf{x}_j \in \tilde{Z}_2 \end{cases} \quad (30)$$

satisfying

$$\mathbf{u}_h(\mathbf{x}) = \begin{cases} \sum_{l=1}^{lP} \hat{\Psi}_l^1(\mathbf{x}) \mathbf{u}_l & \text{if } \mathbf{x}_l \in \tilde{Z}_1, \mathbf{x} \in \Omega_1 \setminus \Omega_2 \\ \sum_{l=1}^{mP} \hat{\Psi}_l^2(\mathbf{x}) \mathbf{u}_l = \sum_{l=1}^{mP} \tilde{\Psi}_l(\mathbf{x}) \mathbf{u}_l & \text{if } \mathbf{x}_l \in \tilde{Z}_2, \mathbf{x} \in \Omega_2 \\ \sum_{l=1}^{lP} \hat{\Psi}_l^1(\mathbf{x}_j) \mathbf{u}_l = \sum_{l=1}^{mP} \hat{\Psi}_l^2(\mathbf{x}_j) \mathbf{u}_l = \mathbf{u}_j & \text{if } \mathbf{x}_j \in \tilde{Z}_2 \end{cases} \quad (31)$$

In general $\hat{\Psi}_l^1(\mathbf{x}) \neq \hat{\Psi}_l^2(\mathbf{x})$ on interface Γ except at the interface nodes $\mathbf{x} = \mathbf{x}_l \in \tilde{Z}_2$. A non-conforming meshfree approximation with point-wise continuity across the interface is illustrated in Fig. 8 for a two dimensional case.

Since the displacement continuity across the interface is only imposed point-wisely at the interface-fitted nodes, the weak form of Eq. (14) is reformulated based on the non-conforming meshfree approximation. We now define immersed meshfree solution of the elastic composite solid problem as a function $\mathbf{u}_h \in \hat{V}_h$ satisfying

$$\hat{\mathbf{a}}(\mathbf{u}_h, \mathbf{v}_h) = \hat{\mathbf{l}}(\mathbf{v}_h), \forall \mathbf{v}_h \in \hat{V}_h \quad (32)$$

where

$$\hat{\mathbf{a}}(\mathbf{u}_h, \mathbf{v}_h) = \underbrace{\int_{\Omega_1 \setminus \Omega_2} \boldsymbol{\varepsilon}(\mathbf{u}_h) \cdot \mathbf{C}^+ \cdot \boldsymbol{\varepsilon}(\mathbf{v}_h) d\Omega + \int_{\Omega_2} \boldsymbol{\varepsilon}(\mathbf{u}_h) \cdot \mathbf{C}^- \cdot \boldsymbol{\varepsilon}(\mathbf{v}_h) d\Omega}_{\text{integrating using integration cells from composite solid}} + \underbrace{\int_{\Omega_2} \boldsymbol{\varepsilon}(\mathbf{u}_h) \cdot (\mathbf{C}^- - \mathbf{C}^+) \cdot \boldsymbol{\varepsilon}(\mathbf{v}_h) d\Omega}_{\text{integrating using integration cells from inclusion}} \quad (33)$$

$$\hat{\mathbf{l}}(\mathbf{v}_h) = \underbrace{\int_{\Omega_1 \setminus \Omega_2} \mathbf{f}^+ \cdot \mathbf{v}_h d\Omega + \int_{\Omega_2} \mathbf{f}^+ \cdot \mathbf{v}_h d\Omega}_{\text{integrating using integration cells from composite solid}} + \underbrace{\int_{\Omega_2} (\mathbf{f}^- - \mathbf{f}^+) \cdot \mathbf{v}_h d\Omega}_{\text{integrating using integration cells from inclusion}} \quad (34)$$

and the associated discrete (broken) energy norm is defined by

$$\|\mathbf{V}_{1,h}\| = \hat{\mathbf{a}}(\mathbf{v}_h, \mathbf{v}_h)^{\frac{1}{2}}, \mathbf{v}_h \in \hat{V}_h \quad (35)$$

Using the Cauchy–Schwarz inequality and triangle inequality, it can be shown that the modified bilinear form $\hat{\mathbf{a}}(\cdot, \cdot)$ is bounded on $\hat{V}_h \times \hat{V}_h$ with respect to the broken energy norm on Ω .

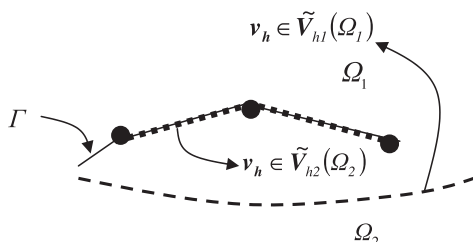


Fig. 7. Non-conforming meshfree approximation near the interface in a two dimensional case.

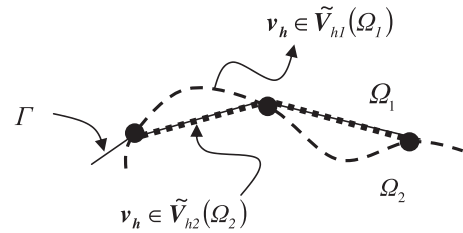


Fig. 8. Point-wise continuity along the interface in a two dimensional case.

Lemma 3.1. There exists a positive constant c_b such that for any $\mathbf{u}_h, \mathbf{v}_h \in \hat{V}_h$, we have

$$|\hat{\mathbf{a}}(\mathbf{u}_h, \mathbf{v}_h)| \leq c_b \|\mathbf{u}_h\|_{1,h} \|\mathbf{v}_h\|_{1,h} \quad (36)$$

Proof.

$$\begin{aligned} |\hat{\mathbf{a}}(\mathbf{u}_h, \mathbf{v}_h)|^2 &= \left| \int_{\Omega_1 \setminus \Omega_2} \boldsymbol{\varepsilon}(\mathbf{u}_h) \cdot \mathbf{C}^+ \cdot \boldsymbol{\varepsilon}(\mathbf{v}_h) d\Omega + \int_{\Omega_2} \boldsymbol{\varepsilon}(\mathbf{u}_h) \cdot \mathbf{C}^- \cdot \boldsymbol{\varepsilon}(\mathbf{v}_h) d\Omega \right. \\ &\quad \left. + \int_{\Omega_2} \boldsymbol{\varepsilon}(\mathbf{u}_h) \cdot (\mathbf{C}^- - \mathbf{C}^+) \cdot \boldsymbol{\varepsilon}(\mathbf{v}_h) d\Omega \right|^2 \\ &\leq \int_{\Omega_1 \setminus \Omega_2} |\boldsymbol{\varepsilon}(\mathbf{u}_h) \cdot \mathbf{C}^+ \cdot \boldsymbol{\varepsilon}(\mathbf{v}_h)|^2 d\Omega + \int_{\Omega_2} |\boldsymbol{\varepsilon}(\mathbf{u}_h) \cdot \mathbf{C}^- \cdot \boldsymbol{\varepsilon}(\mathbf{v}_h)|^2 d\Omega \\ &\leq \gamma_{\max}^+{}^2(\mathbf{C}^+) \left(\int_{\Omega_1 \setminus \Omega_2} \|\boldsymbol{\varepsilon}(\mathbf{u}_h)\|_0^2 d\Omega \right) \left(\int_{\Omega_1 \setminus \Omega_2} \|\boldsymbol{\varepsilon}(\mathbf{v}_h)\|_0^2 d\Omega \right) \\ &\quad + \gamma_{\max}^-{}^2(\mathbf{C}^-) \left(\int_{\Omega_2} \|\boldsymbol{\varepsilon}(\mathbf{u}_h)\|_0^2 d\Omega \right) \left(\int_{\Omega_2} \|\boldsymbol{\varepsilon}(\mathbf{v}_h)\|_0^2 d\Omega \right) \\ &\leq \max\{\gamma_{\max}^+{}^2, \gamma_{\max}^-{}^2\} |\mathbf{u}_h|_{1,h}^2 |\mathbf{v}_h|_{1,h}^2 \\ &\leq c_b^2 \|\mathbf{u}_h\|_{1,h}^2 \|\mathbf{v}_h\|_{1,h}^2 \quad \forall \mathbf{u}_h, \mathbf{v}_h \in \hat{V}_h \quad \square \end{aligned} \quad (37)$$

In inequality (37), we have used the discrete semi-norm on space \hat{V}_h defined by standard Sobolev notation as

$$|\mathbf{v}_h|_{1,h}^2 = |\mathbf{v}_h|_{1,\Omega_1/\Omega_2}^2 + |\mathbf{v}_h|_{1,\Omega_2}^2 \quad (38)$$

The constants γ_{\max}^+ and γ_{\max}^- in inequality (37) are the largest eigenvalues of \mathbf{C}^+ and \mathbf{C}^- respectively.

It is also not difficult to show that the modified bilinear form $\hat{\mathbf{a}}(\cdot, \cdot)$ is positive-definite on \hat{V}_h .

Lemma 3.2. There exists a positive constant c_c such that for any $\mathbf{v}_h \in \hat{V}_h$, we have

$$\hat{\mathbf{a}}(\mathbf{v}_h, \mathbf{v}_h) \geq c_c \|\mathbf{v}_h\|_{1,h}^2 \quad (39)$$

Proof. Observing that $\hat{\mathbf{a}}(\mathbf{v}_h, \mathbf{v}_h) = 0$ implies \mathbf{v}_h is constant. Since \mathbf{v}_h vanishes on global boundary $\partial\Omega$ and satisfies continuity at the interface-fitted nodes, we have $\mathbf{v}_h = 0$ in Ω and thus ensure the coercivity of the modified bilinear form. \square

The uniqueness solution of the discretization problem (32) then follows by the Lax–Milgram theorem.

Theorem 3.1. Let $u \in V$ be the solution of the variational problem (7), the discretization problem (32) in immersed meshfree method admits a uniqueness solution $\mathbf{u}_h \in \hat{V}_h$.

3.3. A degenerated mortar method and energy-norm error estimate

Since $\hat{\mathbf{a}}(\cdot, \cdot)$ is coercive, we can apply the well-known second Strang’s lemma [47] for the energy-norm error estimate.

$$\|\mathbf{u} - \mathbf{u}_h\|_{1,h} \leq C \left\{ \inf_{\mathbf{v} \in \widehat{\mathbf{V}}_h} \|\mathbf{u} - \mathbf{v}\|_{1,h} + \sup_{\mathbf{w}_h \in \widehat{\mathbf{V}}_h \setminus \{0\}} \frac{|\hat{a}(\mathbf{u} - \mathbf{u}_h, \mathbf{w}_h)|}{\|\mathbf{w}_h\|_{1,h}} \right\} \quad (40)$$

where the first term on the R.H.S. of inequality (40) is the best approximation error which can be obtained by the meshfree approximation error estimate and the second term is the consistency error which comes from the non-conforming of $\widehat{\mathbf{V}}_h$. Assume the regularity on the exact solution $\mathbf{u} \in \mathbf{H}^2(\Omega)$, we have the following error estimate by Céa's inequality [52]

$$\inf_{\mathbf{v} \in \widehat{\mathbf{V}}_h} \|\mathbf{u} - \mathbf{v}\|_{1,h} \leq \|\mathbf{u} - \mathbf{I}_h \mathbf{u}\|_{1,h} \leq ch|\mathbf{u}|_{2,\Omega} \quad (41)$$

where h is the largest nodal support radius, i.e., $h = \sup_{I \in \mathcal{Z}_I} \{\text{diam}(r_I)\}$. Note that it is sufficient to choose the inverse tangent basis function and C^2 window function in GMF method to have \mathbf{H}^2 meshfree shape functions. It is also noted that the material constant \mathbf{C} is discontinuous across the interface. Therefore, it is possible that the solution \mathbf{u} of the elasticity interface problem may not be in $\mathbf{H}^2(\Omega)$ due to the rough solution presented in the problem.

Because the interface Γ is associated with a one dimensional triangulation, we call this one dimensional triangulation on Γ , Ξ_h . Each integration segment $e_i \in \Xi_h$ is a boundary edge of integration cell (finite element triangulation) T_{h_2} in Ω_2 . For the consistency error, we use the definition of $\hat{a}(\cdot, \cdot)$ in Eq. (33) and Galerkin orthogonality together with Green's theorem to yield

$$\begin{aligned} \hat{a}(\mathbf{u} - \mathbf{u}_h, \mathbf{w}_h) &= \hat{a}(\mathbf{u}, \mathbf{w}_h) - \hat{l}(\mathbf{w}_h) \\ &= \int_{\Omega_1 \setminus \Omega_2} \nabla \cdot (\mathbf{C}^+ \cdot \nabla_s \mathbf{u}) \cdot \mathbf{w}_h d\Omega \\ &\quad + \int_{\Omega_2} \nabla \cdot (\mathbf{C}^- \cdot \nabla_s \mathbf{u}) \cdot \mathbf{w}_h d\Omega - \int_{\Omega} \mathbf{f} \cdot \mathbf{w}_h d\Omega \\ &= \int_{\Omega_1 \setminus \Omega_2} \nabla \cdot (\mathbf{C}^+ \cdot \nabla_s \mathbf{u}) \cdot \mathbf{w}_h d\Omega \\ &\quad + \int_{\Omega_2} \nabla \cdot (\mathbf{C}^- \cdot \nabla_s \mathbf{u}) \cdot \mathbf{w}_h d\Omega \\ &\quad - \left(\int_{\Omega_1 \setminus \Omega_2} \nabla \cdot (\mathbf{C}^+ \cdot \nabla_s \mathbf{u}) \cdot \mathbf{w}_h d\Omega \right. \\ &\quad \left. + \int_{\Omega_2} \nabla \cdot (\mathbf{C}^- \cdot \nabla_s \mathbf{u}) \cdot \mathbf{w}_h d\Omega \right. \\ &\quad \left. - \int_{\Gamma} \mathbf{C} \cdot \boldsymbol{\varepsilon}(\mathbf{u}) \cdot \mathbf{n} \cdot \mathbf{w}_h d\Gamma \right) \\ &= \sum_{e_i \in \Xi_h} \int_{e_i} (\mathbf{C} \cdot \boldsymbol{\varepsilon}(\mathbf{u}) \cdot \mathbf{n}) \cdot \llbracket \mathbf{w}_h \rrbracket ds \end{aligned} \quad (42)$$

where the term $\int_{e_i} (\mathbf{C} \cdot \boldsymbol{\varepsilon}(\mathbf{u}) \cdot \mathbf{n}) \cdot \llbracket \mathbf{w}_h \rrbracket ds$ can be realized as the weak constraint equation appearing in the Lagrange multiplier-type mortar method in which $\lambda_h = \mathbf{C} \cdot \boldsymbol{\varepsilon}(\mathbf{u}) \cdot \mathbf{n} \in (L^2(\Gamma))^2$ are Lagrange multipliers. The symbol $\llbracket \mathbf{w} \rrbracket$ denotes the restriction of jump as defined in Eq. (2) for $\mathbf{w} \in \Gamma$. A natural choice for the construction of Lagrange multiplier spaces in non-conforming formulation of the mortar method is to define the Lagrange multiplier basis function locally associated with the discrete nodes. From this point of view, we regard the proposed embedded meshfree method as a degenerated Lagrange multiplier-type mortar method due to the fact that the displacement jump vanishes at the interface-fitted nodes, i.e.,

$$\llbracket \mathbf{w}_h \rrbracket_I = (\mathbf{w}_I^+ - \mathbf{w}_I^-) = 0 \quad \forall I \in \widetilde{\mathcal{Z}}_2 \quad (43)$$

Applying the point collocation method to the assembly of discrete constraint equation in mortar method and using Eq. (42) lead to the primal problem presented in Eq. (32).

$$\begin{aligned} \hat{a}(\mathbf{u}, \mathbf{w}_h) - \hat{l}(\mathbf{w}_h) &= \sum_{e_i \in \Xi_h} \int_{e_i} \mathbf{C} : \boldsymbol{\varepsilon}(\mathbf{u}) \cdot \mathbf{n} \cdot \llbracket \mathbf{w}_h \rrbracket ds \\ &= \sum_{e_i \in \Xi_h} \sum_{I=1}^2 \mathbf{C} \cdot \boldsymbol{\varepsilon}(\mathbf{u}^I) \cdot \mathbf{n}_I \cdot (\mathbf{w}_I^+ - \mathbf{w}_I^-) = 0 \quad \forall \mathbf{w}_h \in \widehat{\mathbf{V}}_h \end{aligned} \quad (44)$$

Despite the vanishing constraint equation in the primal problem, the proposed immersed meshfree method still presents certain boundary quadrature error by different quadrature rules and requires a consistency error estimate to ensure a stable and convergent meshfree discretization. This consistency error estimate resembles that of meshfree solution in standard Galerkin meshfree method using moving least-squares approximation [36], or reproducing kernel approximation [37], when Dirichlet boundary conditions are imposed in point-wise fashion.

Lemma 3.3. Assume that $u \in H^2(\Omega)$ be the solution of elastic composite solid problem in Eq. (7), there exists a constant c_c independent of h and function u such that

$$|\hat{a}(\mathbf{u}, \mathbf{w}_h) - \hat{l}(\mathbf{w}_h)| \leq c_c h |u|_2 \|\mathbf{w}_h\|_{1,h} \quad \forall \mathbf{w}_h \in \widehat{\mathbf{V}}_h \quad (45)$$

Proof. Let D_{n^\pm} denotes the normal derivative in the sense of trace at the interface Γ with the label “ \pm ” represents the limit of quantities at each side of the interface and is defined by

$$D_{n^\pm} \mathbf{u}^\pm = \sum_{ij} C_{ij}^\pm \frac{\partial \mathbf{u}^\pm}{\partial X_j} n_i \quad (46)$$

where $u = u^+ = u^-$, $\mathbf{C} = (C_{ij})_{2 \times 2}$ is the material coefficient matrix and \mathbf{n} is the outward unit normal vector on Γ as defined in Section 2. According to the homogenous Neumann jump condition, we have $D_n \mathbf{u} = D_{n^+} \mathbf{u}^+ = D_{n^-} \mathbf{u}^-$ on material interface Γ . Using Eqs. (42) and (46) and Cauchy–Schwarzs inequality followed by standard trace inequality, we have

$$\begin{aligned} |\hat{a}(\mathbf{u}, \mathbf{w}_h) - \hat{l}(\mathbf{w}_h)| &= \left| \sum_{e_i \in \Xi_h} \int_{e_i} (\mathbf{C} \cdot \boldsymbol{\varepsilon}(\mathbf{u}) \cdot \mathbf{n}) \cdot \llbracket \mathbf{w}_h \rrbracket ds \right| \\ &\leq \sum_{e_i \in \Xi_h} \left(\int_{e_i} |D_n \mathbf{u}| \|\llbracket \mathbf{w}_h \rrbracket\| ds \right) \\ &\leq \sum_{e_i \in \Xi_h} \left(\int_{e_i} |D_n \mathbf{u}| ds \right) \left(\int_{e_i} |\mathbf{w}_h^+ - \mathbf{w}_h^-| ds \right) \\ &\leq \sum_{e_i \in \Xi_h} \left(\int_{e_i} |D_n \mathbf{u}| ds \right) \left(\int_{e_i} |\mathbf{w}_h^+| ds + \int_{e_i} |\mathbf{w}_h^-| ds \right) \\ &\leq \sum_{e_i \in \Xi_h} |e_i|^{1/2} \left(\int_{e_i} |D_n \mathbf{u}|^2 ds \right)^{1/2} \\ &\quad \times |e_i|^{1/2} \left\{ \left(\int_{e_i} |\mathbf{w}_h^+|^2 ds \right)^{1/2} + \left(\int_{e_i} |\mathbf{w}_h^-|^2 ds \right)^{1/2} \right\} \\ &\leq c_{c1} h \|D_n \mathbf{u}\|_{0,\Gamma} \left(\|\mathbf{w}_h^+\|_{0,\Gamma} + \|\mathbf{w}_h^-\|_{0,\Gamma} \right) \\ &\leq c_{c1} h \|D_n \mathbf{u}\|_1 \left(\|\mathbf{w}_h\|_{1,\Omega_1/\Omega_2} + \|\mathbf{w}_h\|_{1,\Omega_2} \right) \\ &\leq c_c h |u|_2 \|\mathbf{w}_h\|_{1,h} \quad \square \end{aligned} \quad (47)$$

where we have related the largest nodal support radius h to the maximum length of element edge e_i along the interface Γ by defining

$$\exists c_1 \geq 1, h = \sup_{I \in \mathcal{Z}_I} h_I = \sup_{I \in \mathcal{Z}_I} (\text{diam } \mathbf{r}_I) = c_1 \sup_{e_j \in \Gamma} |e_j| \quad (48)$$

Lemma 3.3 implies

$$\sup_{\mathbf{w}_h \in \widehat{\mathbf{V}}_h \setminus \{0\}} \frac{|\hat{a}(\mathbf{u}, \mathbf{w}_h) - \hat{l}(\mathbf{w}_h)|}{\|\mathbf{w}_h\|_{1,h}} \leq c_c h |\mathbf{u}|_2 \quad (49)$$

This indicates that the estimate of consistency error for the immersed meshfree method is of $O(h)$. Combining inequalities (40), (41) and (49), we obtain the following result for the energy error.

Proposition 3.1. *Let $u \in H^2(\Omega)$ and $\mathbf{u}_h \in \widehat{\mathbf{V}}_h$ be respectively the solutions of the weak problem (7) and of the discretized problem (32). Then it holds*

$$\|\mathbf{u} - \mathbf{u}_h\|_{1,h} \leq h |\mathbf{u}|_2 \quad (50)$$

By Proposition 3.1, we expect the optimal rate of convergence for immersed meshfree method to be one for u in $H^2(\Omega)$.

4. Numerical procedures and discrete equations

To perform a composite solid analysis using the proposed method, typical inclusions of realistic morphology such as reinforced particles or fibers are idealized. For example in microscopic analysis, the realistic morphology can be constructed using several

visualization techniques such as atomic force microscopy (AFM), X-ray tomography and serial sectioning [53,54]. Those inclusions can be digitized and segmented into multiple regions (sets of pixels). The segmentation of these regions in voxel-based mesh requires further smoothing and idealization to identify their boundaries. More precisely, the segmentation process is utilized to define the iso-surface of composite solid and therefore the boundaries of inclusions as illustrated in Fig. 9. Once the iso-surface is formed, a surface triangulation technique can be used to discretize the material interface. From there, a marching cubes algorithm [55] (or marching squares in 2D) is adopted to construct the conforming meshes across the material interface. Unfortunately, constructing a conforming mesh for the finite element analysis of idealized composite involving multiple and complex inclusions may be very time consuming and sometimes is impossible to achieve. In order to construct a conforming mesh, most of time the idealized inclusions have to be further simplified and therefore lose their practical applicability. As a result, establishing an efficient approach to handle the geometrical interaction becomes important and remains a challenging task for the macro and micromechanical modeling of composite solids.

The procedures of immersed meshfree analysis of composite solid start with embedding the inclusion into the base material. Since

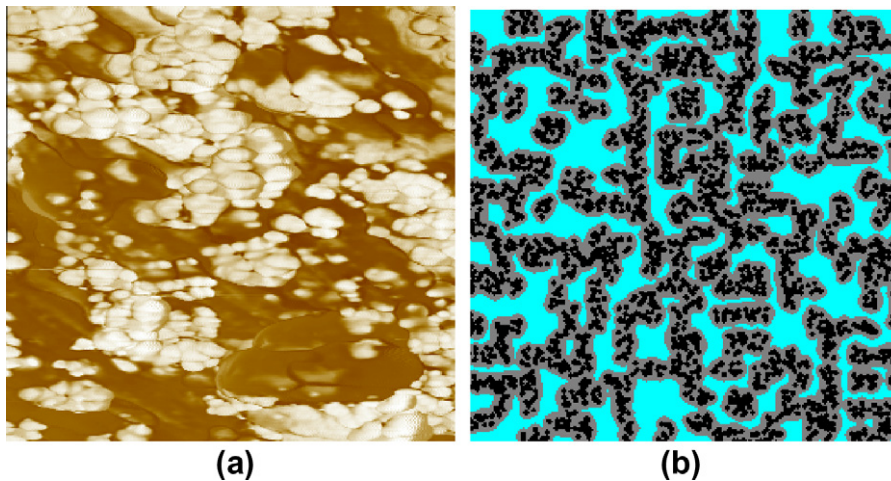


Fig. 9. Example of an idealization process in particle-reinforced composite. (a) AFM image. (b) Idealized composite solid.

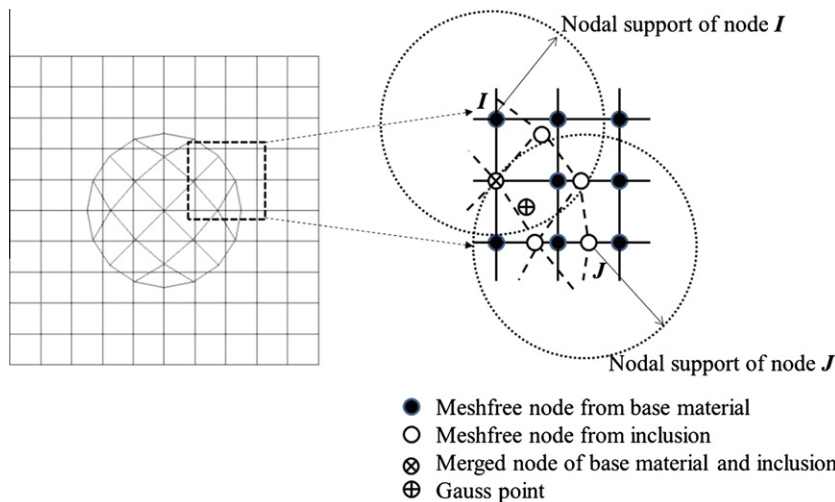


Fig. 10. Illustration of integration cells in computation domain Ω_1 of composite solid.

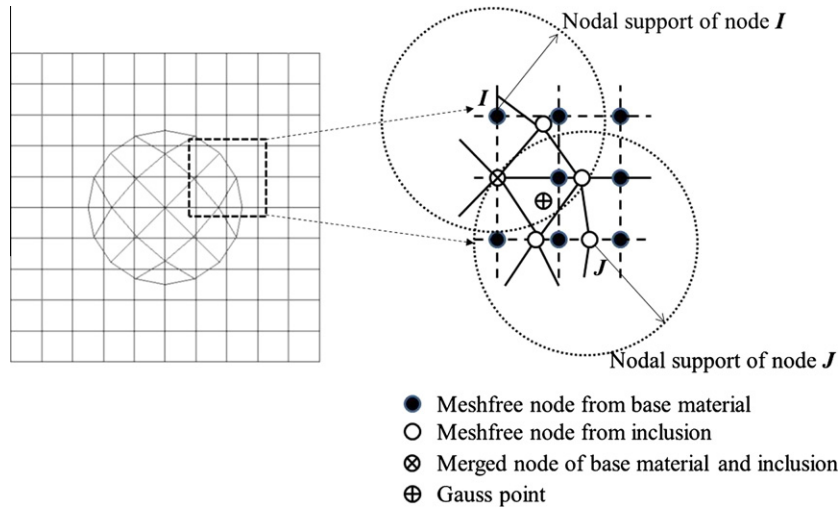


Fig. 11. Illustration of integration cells in computation domain Ω_2 of inclusion.

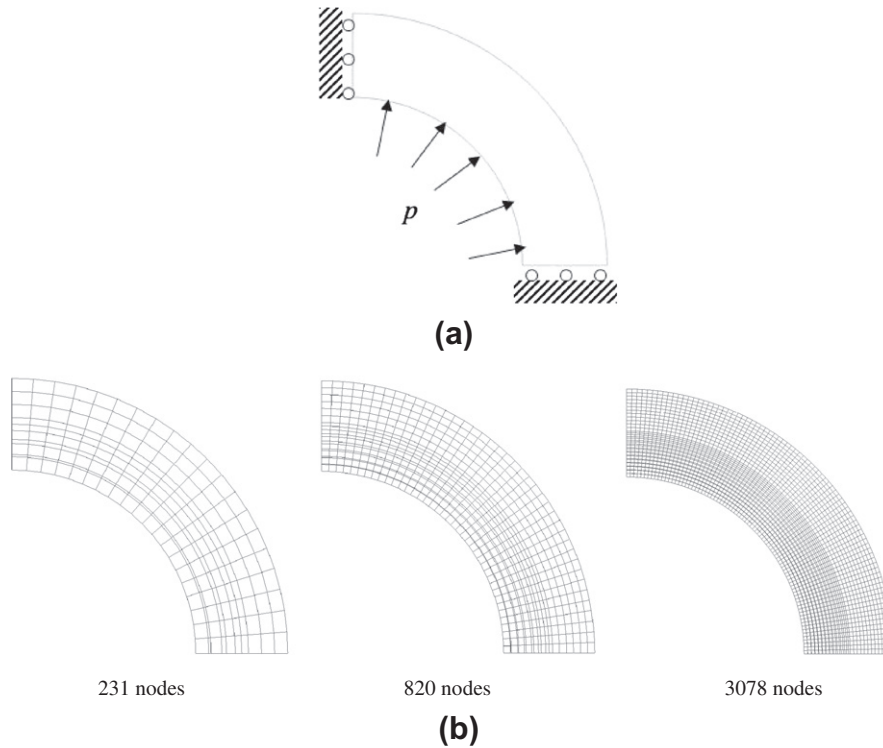


Fig. 12. Pressure vessel problem. (a) Geometry and boundary condition. (b) Three levels of immersed meshfree discretizations.

information regarding the geometry of material interface is stored in the geometrical model of inclusions, the solid mesh generation for inclusions can be as detail as possible to better represent realistic morphology. The mesh generation of the base material can be independent of that in the inclusions. In other words, a structured mesh can be easily generated for the base material, and material interface does not need to be considered in this step. This nice feature avoids the necessity of additional unknowns in the extrinsic finite element methods such as extended finite element method. To perform a meshfree analysis, displacement approximations in Section 3 of the paper are rewritten in the following form:

$$\mathbf{u}_h(\mathbf{x}) = \begin{cases} \sum_{l=1}^{LP} \hat{\Psi}_l^1(\mathbf{x}) \mathbf{u}_l & \text{if } \mathbf{x}_l \in \tilde{Z}_1 = \{\tilde{\mathbf{x}}_l, l = 1, \dots, LP\}, \mathbf{x} \in \Omega_1 \setminus \Omega_2 \\ \sum_{l=1}^{MP} \hat{\Psi}_l^2(\mathbf{x}) \mathbf{u}_l = \sum_{l=1}^{MP} \tilde{\Psi}_l(\mathbf{x}) \mathbf{u}_l & \text{if } \mathbf{x}_l \in \tilde{Z}_2 = \{\tilde{\mathbf{x}}_l, l = 1, \dots, MP\}, \mathbf{x} \in \Omega_2 \\ \sum_{l=1}^{LP} \hat{\Psi}_l^1(\mathbf{x}_j) \mathbf{u}_l = \sum_{l=1}^{MP} \hat{\Psi}_l^2(\mathbf{x}_j) \mathbf{u}_l = \mathbf{u}_j & \text{if } \mathbf{x}_j \in \tilde{Z}_2 \end{cases} \quad (51)$$

where MP is the total number of overlapping nodes in sub-region Ω_2 which is the computation domain of inclusion. $LP=NP-MP+IP$ denotes total number of overlapping nodes in sub-region $\Omega_1 \setminus \Omega_2$

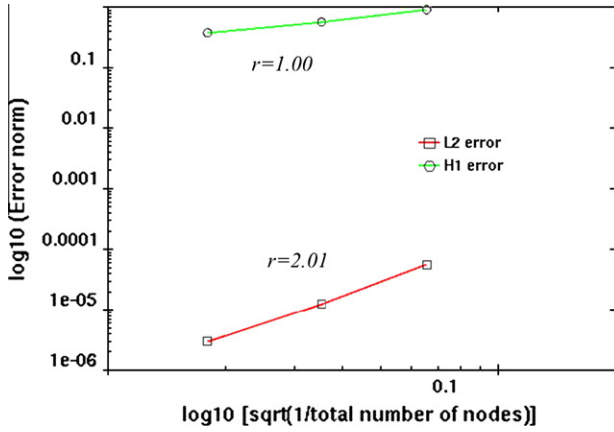


Fig. 13. L^2 and H^1 error norms in pressure vessel model.

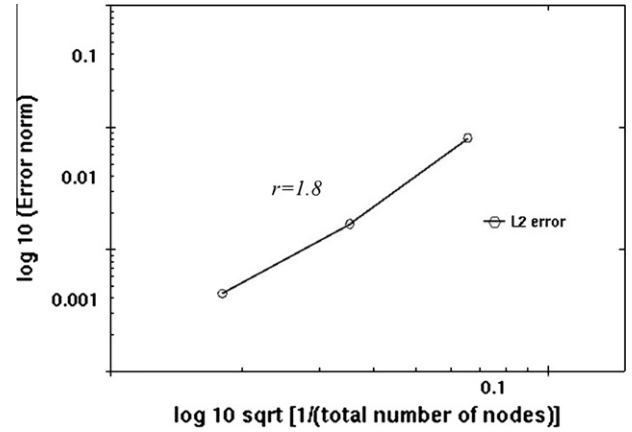


Fig. 15. L^2 error norms of interface traction.

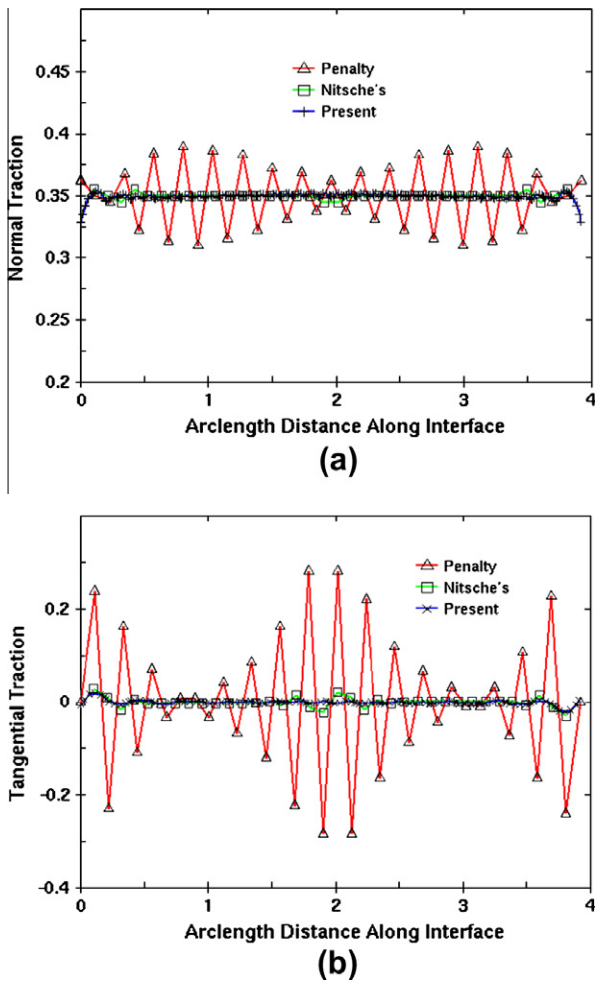


Fig. 14. Comparison of traction along interface. (a) Normal traction. (b) Tangential traction.

which represents the computation domain of base material. NP is the total number of overlapping nodes in sub-region Ω_1 and IP is total number of interface-fitted nodes usually obtained from the discretization in inclusion. $\hat{\Psi}_l^1$ and $\hat{\Psi}_l^2$ are meshfree shape functions in sub-regions $\Omega_1 \setminus \Omega_2$ and Ω_2 respectively. The corresponding discrete equations of variational formulation are used to perform the numerical integration and are given by

$$\hat{\mathbf{K}}\mathbf{d} = \mathbf{f}^{ext} \quad (52)$$

$$\hat{\mathbf{K}} = \hat{\mathbf{K}}^1 + \hat{\mathbf{K}}^2 \quad (53)$$

$$\mathbf{f}^{ext} = \hat{\mathbf{f}}^1 + \hat{\mathbf{f}}^2 \quad (54)$$

$$\hat{\mathbf{K}}_{ij}^1 = \sum_{m=1}^{n1} \sum_{n=1}^{int \times int} \hat{\mathbf{B}}_i^T(\mathbf{x}_n) \mathbf{C}^+ \hat{\mathbf{B}}_j(\mathbf{x}_n) A_{mn} \quad (55)$$

$$\hat{\mathbf{K}}_{ij}^2 = \sum_{m=1}^{n2} \sum_{n=1}^{int \times int} \hat{\mathbf{B}}_i^T(\mathbf{x}_n) (\mathbf{C}^- - \mathbf{C}^+) \hat{\mathbf{B}}_j(\mathbf{x}_n) A_{mn} \quad (56)$$

$$\hat{\mathbf{f}}_i^1 = \sum_{m=1}^{n1} \sum_{n=1}^{int \times int} \hat{\Psi}_l(\mathbf{x}_n) \mathbf{f}^+(\mathbf{x}_n) A_{mn} \quad (57)$$

$$\hat{\mathbf{f}}_i^2 = \sum_{m=1}^{n2} \sum_{n=1}^{int \times int} \hat{\Psi}_l^2(\mathbf{x}_n) (\mathbf{f}^-(\mathbf{x}_n) - \mathbf{f}^+(\mathbf{x}_n)) A_{mn} \quad (58)$$

$$\hat{\mathbf{B}}_l(\mathbf{x}) = \begin{cases} \hat{\mathbf{B}}_l^1(\mathbf{x}) & \text{if } \mathbf{x}_l \in \tilde{Z}_1 = \{\tilde{\mathbf{x}}_l, l = 1, \dots, LP\}, \mathbf{x} \in \Omega_1 \setminus \Omega_2 \\ \hat{\mathbf{B}}_l^2(\mathbf{x}) & \text{if } \mathbf{x}_l \in \tilde{Z}_2 = \{\tilde{\mathbf{x}}_l, l = 1, \dots, MP\}, \mathbf{x} \in \Omega_2 \end{cases} \quad (59)$$

where n_1 is the total number of integration cells in computation domain Ω_1 of composite solid and n_2 is the total number of integration cells in the computation domain Ω_2 of inclusion. The integration cells in Ω_1 and Ω_2 are plotted in solid line and illustrated in the subplots of zoomed-in area in Figs. 10 and 11 respectively. \mathbf{C}^+ and \mathbf{C}^- are elasticity tensors of base material and inclusion respectively. The discrete equations are evaluated at Gauss point \mathbf{x}_n with $int \times int$ Gauss quadrature rule in each integration cell. The symbol A_{mn} denotes the corresponding weighted area of n th Gauss point in m th integration cell. $\hat{\mathbf{B}}_l^j, j = 1, 2$ is standard \mathbf{B} -matrix of node l defined according to Eq. (51).

The numerical procedures are summarized as follows:

- (1) Generating the solid mesh for digitized and idealized inclusions obtained from visualization technique.
- (2) Generating the structured solid mesh for composite solid that does not contain the geometrical information of inclusions and the associated material interface.
- (3) Embedding the mesh in step (1) into the mesh in step (2).
- (4) Merging the coincided nodes to form a set of distinct nodes for meshfree approximation.
- (5) Constructing displacement approximation according to Eq. (51).
- (6) Performing numerical integration in Eqs. (52)–(58) and enforcing global boundary conditions for macro or micromechanical analysis.

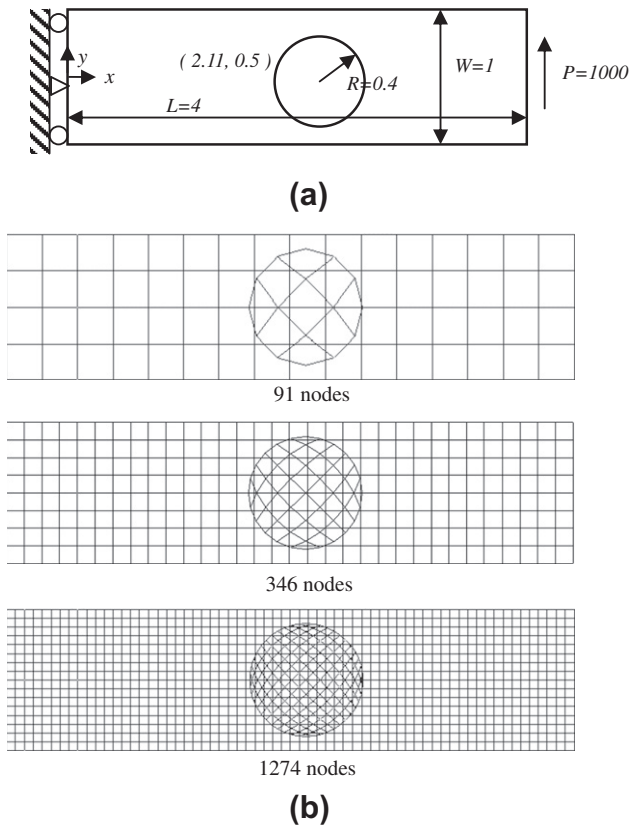


Fig. 16. Cantilever beam problem. (a) Geometry and boundary conditions. (b) Three levels of immersed meshfree discretizations.

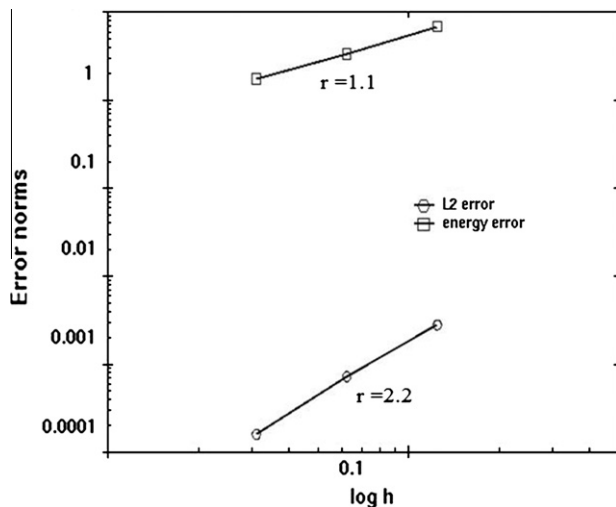


Fig. 17. L^2 and energy error norms in single material model.

5. Numerical examples

In this section, we analyze three simplified-particle models in two-dimension to study the performance of the proposed method in the composite solid problems. Unless otherwise specified, the following conditions are considered: (1) The weight function is chosen to be the cubic B-spline kernel function with normalized support size equal to 1.6 for the construction of meshfree shape functions. (2) A six-point Gauss quadrature rule is used in each

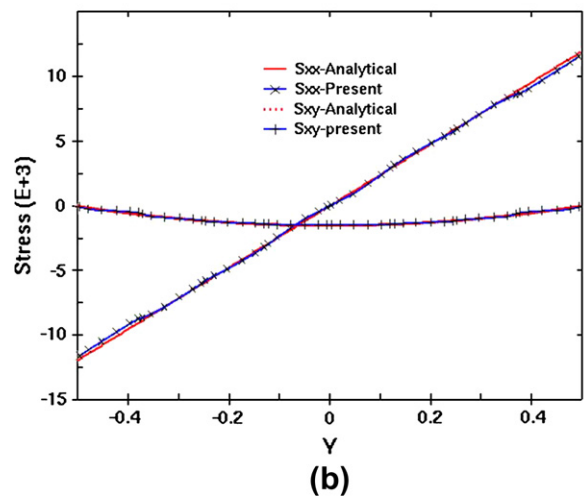
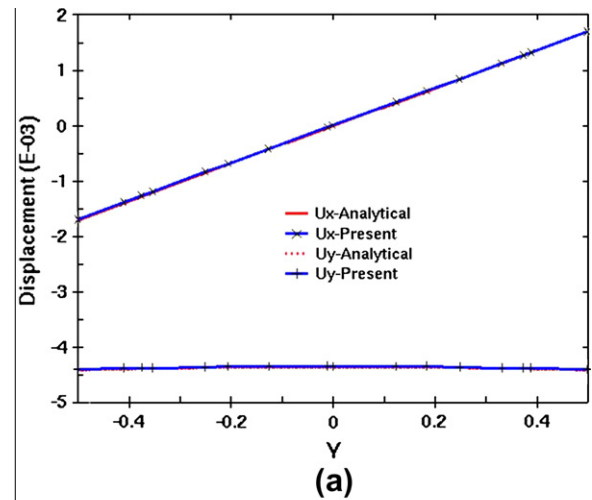


Fig. 18. Distribution of displacements along the cross-section $x = 2.11$ and stresses along the cross-section $x = 2.01$ in single material model (346 nodes). (a) Displacements and (b) stresses.

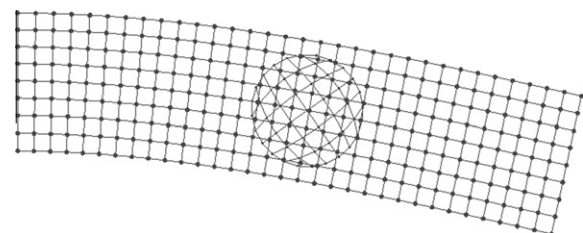


Fig. 19. Deformation plot in single material model (displacement scaled by 50 times): analytical (mesh), numerical (black dot).

integration cell for all examples. (3) The materials are considered to be compressible with Poisson's ratio $\nu = 0.3$ for all two-dimensional cases. (4) For convenience, dimensionless unit system is adopted in this paper. (5) All contour plots are reported at the nodes for the displacement field and at Gauss points for the stress field.

5.1. Pressure vessel

In this example, a two-dimensional thick-walled cylindrical vessel with inner radius $r_1 = 2.0$ and outer radius $r_2 = 3.0$ is

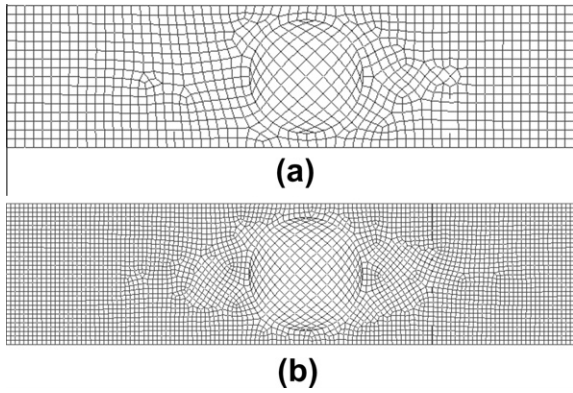


Fig. 20. Two conforming finite element meshes. (a) 1074 nodes. (b) 4055 nodes.

Table 1
The convergence study in composite cantilever beam.

	Energy norm	L^2 norm	Tip displacement
Present			
91 Nodes	3.3941	1.1480E-02	-1.1450E-02
346 Nodes	3.3801	1.1352E-02	-1.1386E-02
1274 Nodes	3.3708	1.1338E-02	-1.1299E-02
FEM			
4055 Nodes	3.3700	1.1336E-02	-1.1290E-02
1074 Nodes	3.3669	1.1320E-02	-1.1272E-02

subjected to a uniform pressure p on the interior wall. An interface is defined at a radius of $r = 2.5$. Due to symmetry of the model, only the upper quadrant of the problem is modeled as described in Fig. 12a. Three levels of overlapping finite element meshes shown in Fig. 12b are used for the convergence study in the proposed method. In order to provide an analytical solution for the

convergence study, we further assume the vessel is made of single material and is under plane stress condition. Under those assumptions, we have the following analytical solutions expressed in polar coordinate system:

The circumferential displacement is $u_\theta = 0$ and radial displacement is

$$u_r = \frac{(1 + \nu)r_1^2 p}{E(r_2^2 - r_1^2)} \left[\frac{(1 - 2\nu)r}{1 + \nu} + \frac{r_2^2}{r^2} \right] \quad (60)$$

where the material properties of the vessel are: Young's modulus $E = 1000.0$ and Poisson's ratio $\nu = 0.0$. The corresponding circumferential and radial stresses are

$$\sigma_r = \frac{pr_1^2(r^2 + r_2^2)}{r^2(r_2^2 - r_1^2)} \quad (61)$$

$$\sigma_\theta = \frac{pr_1^2(r^2 - r_2^2)}{r^2(r_2^2 - r_1^2)} \quad (62)$$

The convergence test is first conducted and the results are reported in Fig. 13. The results of L_2 -norm and H_1 -norm errors are very close to theoretical rate of convergence. To compare with the existing finite element method, the results of extended finite element method in [56] with two tied constraint methods (penalty method and Nitsche's method) are used for comparison. The stress responses along the interface are studied using those methods. Fig. 14a and b depict the normal and tangential tractions of finite element penalty method, finite element Nitsche's method and the proposed method using same level of discretization on the interface. The results of the proposed method are comparable to those of finite element Nitsche's method. On the other hand, the finite element penalty method suffers from a severe numerical oscillation in both normal and tangential tractions and behaves the worst among three methods. The L_2 -norm convergence of the traction fields along the interface using the proposed method is shown in Fig. 15. The results in

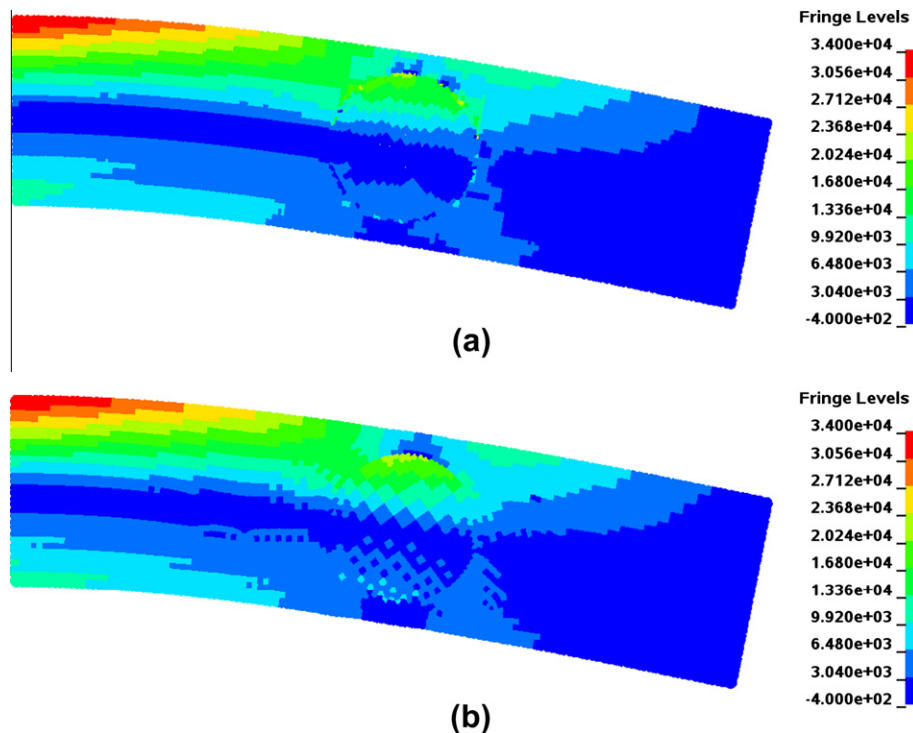


Fig. 21. Maximum principle stress contour on deformed plot (scaled by 50 times) in composite solid model. (a) Present solution (346 nodes). (b) Reference solution from conforming finite element mesh (1074 nodes).

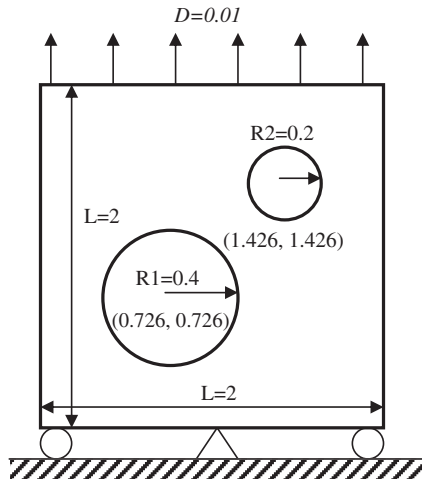


Fig. 22. Graphical presentation of multiple inclusions in the unit cell model.

Figs. 13 and 15 suggest the proposed method converges as the model is refined in the composite solid problem.

5.2. Cantilever beam

In this example, accuracy and convergence of a beam problem for both single and composite solid models are studied. The problem statement and boundary conditions of the beam problem are given in Fig. 16a. For a single material model, it is assumed that the material contains only base matrix with Young's modulus $E^+ = 2.0e+07$. Three regularly refined meshfree discretizations for the beam model are shown in Fig. 16b.

The single material model is first analyzed using the overlapping mesh to verify the theoretical rate of convergence derived in the previous section. Since the beam is composed of one material, analytical solution of the beam problem is available [57]. The results of L^2 -norm and energy-norm errors against the element size are shown in Fig. 17. The proposed method achieves an optimal rate of convergence in both L^2 -norm and energy-norm errors. Fig. 18a displays the distribution of displacement along the cross-section $x = 2.11$ and compares with the analytical solution. Both displacement components are in good agreements with the analytical solution. Fig. 18b compares the stresses distribution with the analytical solution along the cross-section $x = 2.01$ and

good agreements are obtained. A more detailed comparison of displacement solution is shown in Fig. 19. Black dots in this figure denote the nodal locations obtained from the immersed meshfree method, while the mesh represents the analytical solution. In both solutions, the displacements are scaled by a factor of 50. Superior performance of the proposed method is apparent in this deformation plot.

In the composite solid model, we have chosen the Young's modulus of inclusion to be $E^- = 2.0e+10$ which is 1000 times higher than that of base matrix. Since the exact solution is not available, two reference solutions are generated from the conforming finite element method using the standard displacement-based bilinear element formulation. Two finite element meshes shown in Fig. 20a and b represent two level of mesh refinement that conform to the bi-material interface with total number of 1074 and 4055 nodes respectively.

A comparison of energy norm, L^2 norm and tip displacement using the immersed meshfree method and conforming finite element method are listed in Table 1. As shown in Table 1, the immersed meshfree solution converges to the finite element solution of the most refined mesh. Furthermore, the prediction of immersed meshfree method using a coarser discretization is comparable to the finite element solution with a finer mesh. Fig. 21a and b shows the comparison of maximum principle stress distribution in immersed meshfree method using 346 nodes and conforming finite element method using 1074 nodes respectively. The stress contours are plotted on a deformed configuration with the scale factor of 50 in the displacement field. As shown in the comparison, the immersed meshfree method predicts similar results for the maximum principle stress.

5.3. Tensile test in unit cell model with multiple inclusions

In this example, a plane strain tensile test of a unit cell model at the microscopic level is analyzed. The geometry and boundary conditions of unit cell are shown in Fig. 22. The model is composed of a base matrix with Young's modulus $E^+ = 1.0e+05$ and two inclusions with Young's modulus $E^- = 1.0e+08$. The two inclusions are of different sizes and on different locations to represent influence of the morphology of inclusions. The volume fraction of the inclusions is about 15.7% in this test. An overlapping finite element mesh, which includes a structured mesh for base matrix and two semi-uniform meshes for inclusions, is used for the discretization as well as served as the integration cells in the immersed meshfree method. The meshes for the base matrix and two inclusions are constructed

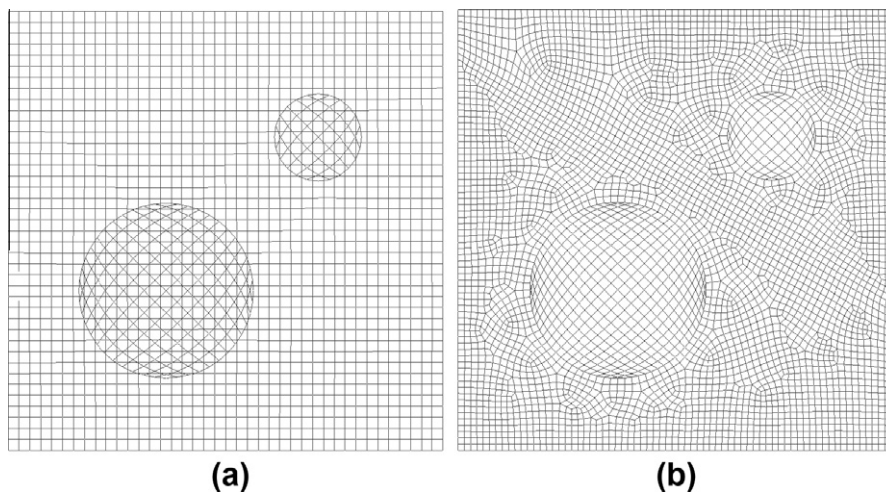


Fig. 23. Discretizations in unit cell model. (a) Immersed meshfree discretization (1899 nodes). (b) Refined conforming finite element mesh (4552 nodes)

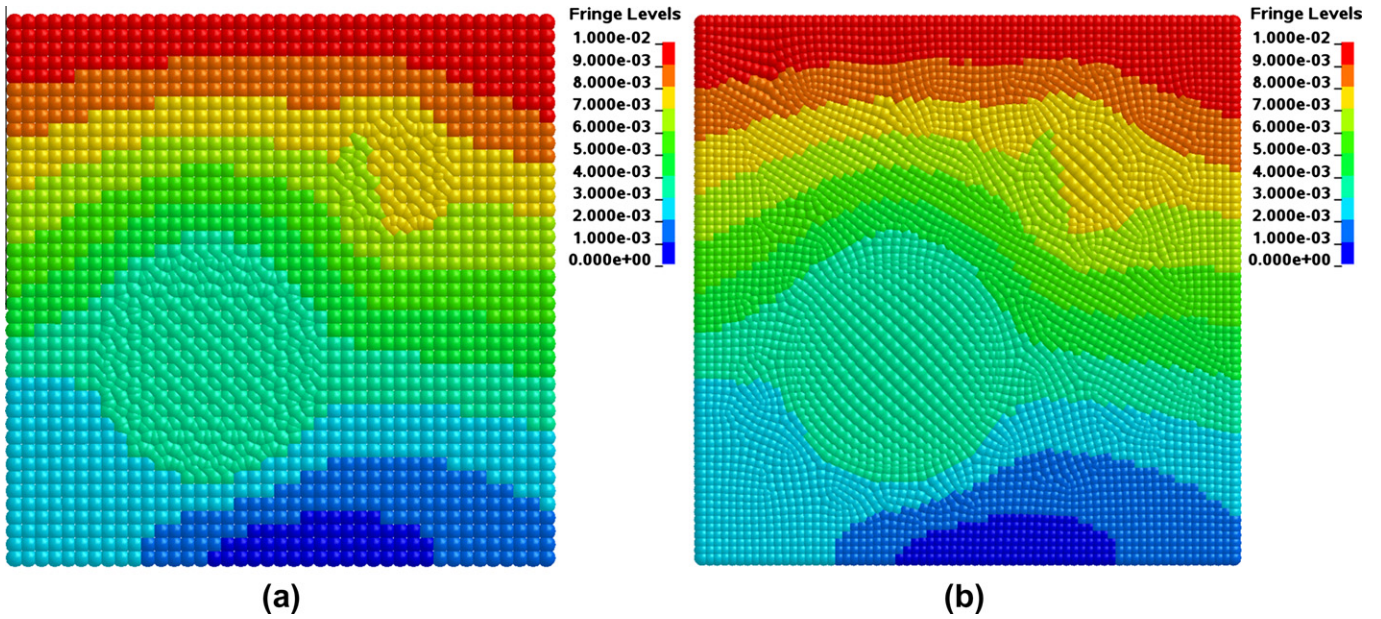


Fig. 24. Effective displacement contour on undeformed plot in unit cell model. (a) Present solution. (b) Reference solution.

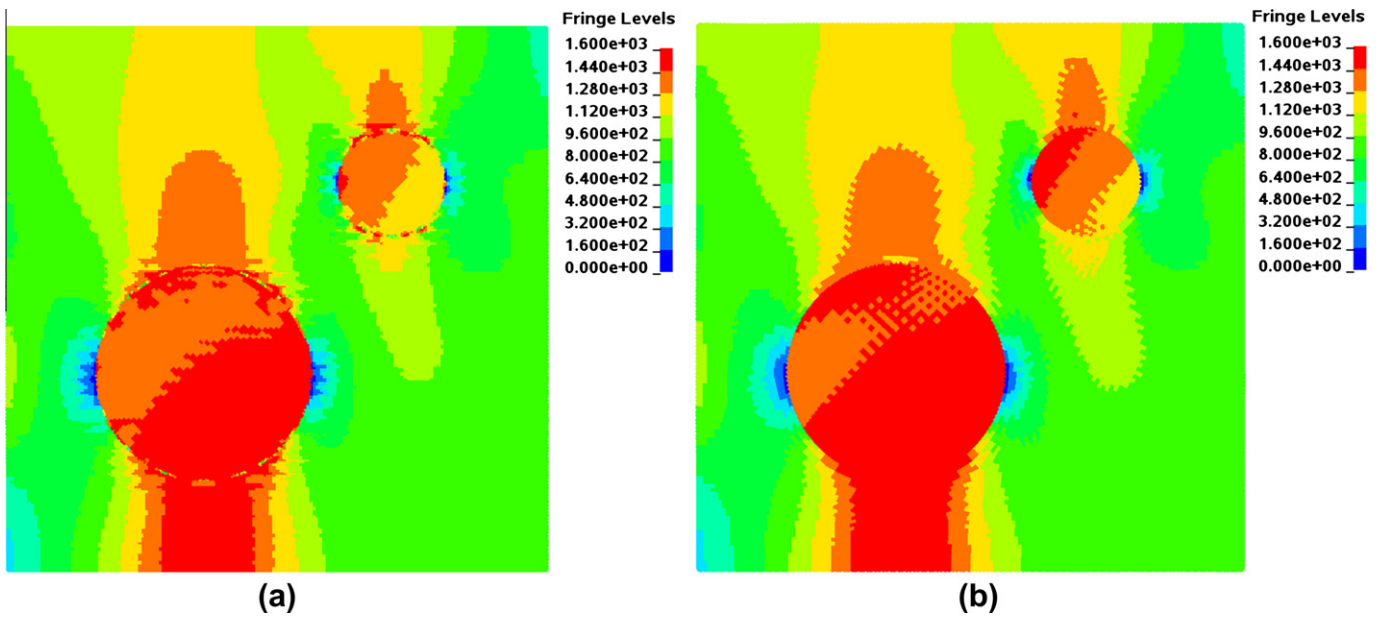


Fig. 25. Maximum principle stress contour on undeformed plot in unit cell model. (a) Present solution. (b) Reference solution.

independently and are easily placed in the computational domain. This model contains a total number of 1899 nodes as shown in Fig. 23a. For comparison, a conforming finite element mesh shown in Fig. 23b is analyzed using a standard displacement-based bilinear element formulation similar to the one in the previous example.

Fig. 24 presents a comparison of displacement fields in the immersed meshfree method and conforming finite element method. The displacement contour in Fig. 24 is expressed in terms of the effective displacement which is computed at discrete nodes and defined by

$$\bar{u}_l = \sqrt{u_{x,l}^2 + u_{y,l}^2} \tag{63}$$

As shown in Fig 24a and b, the immersed meshfree method displays a good performance in the coarse model as compared to the reference solution obtained from finite element method using the fine mesh. A comparison of L^2 norm with a value of $1.1304e-02$ in the immersed meshfree solution and $1.1303e-02$ in the finite element solution suggests that the proposed method is capable of delivering a good displacement solution for the elasticity interface problem. The comparison of maximum principle stress contour is shown in Fig. 25. The stress solution of the immersed meshfree method shown in Fig. 25a is comparable to the stress result obtained from the finite element solution shown in Fig. 25b. The energy norms obtained from the immersed meshfree method and finite element methods are 3.7459 and 3.7511 respectively which differs by a value of 0.1%.

6. Conclusions

In this paper, we proposed and analyzed an immersed meshfree method for the elasticity of composite solid problems. This method introduces a new discretization based on the naturally conforming property of meshfree method to approximate the overlapping sub-domains in the composite solid analyses. The method is regarded as a non-conforming method which can be related to the Lagrangian-type mortar method in treating the material discontinuity across the interface. In contrast to the existing Lagrangian-type mortar finite element and mortar meshfree methods, the proposed approach eliminates the interface constraint equation explicitly from the variational formulation. It introduces a new meshfree discretization and a point-wise continuity across the material interface, thus eliminating the need for control or stabilization parameters. This unique property offers great flexibility over other methods with respect to adoption of overlapping mesh in the composite solid analyses. Theoretical results such as uniform ellipticity and consistency error are given in separate lemmas. Optimal energy norm error estimate is derived and is further illustrated by numerical experiments.

Three two-dimensional composite solid examples are provided to examine the effectiveness and accuracy of the proposed method. Our numerical results indicate that the numerical convergence rate of the proposed method is close to the theoretical rate of convergence, and the solution using relatively coarse discretization is comparable with that obtained from the finite element method using a fine and conforming mesh. Compared to the extrinsic finite element approaches using level set method in defining the implicit material interface, the proposed method does not require additional degrees of freedom to model the interface problem and results in a symmetric, positive-definite system of equations. As a result, the proposed method is exempted from the need for a nodal enrichment procedure and subsequently the need for the sub-triangulation scheme in the extrinsic approaches. This nice feature simplifies the numerical implementation of the proposed method in the standard displacement-based meshfree Galerkin code and may prove particularly useful within the context of large-scale model containing multiple and aggregated inclusions in particular for three-dimensional problems. An extension of present study to the large-scale, nonlinear, interface de-bonding and three-dimensional problems is under investigation. To improve the computation cost in three-dimensional meshfree analysis, attempts such as the introduction of meshfree-enriched finite element approximation [45] to the interface-fitted nodes will be investigated.

Acknowledgements

The authors would like to thank Dr. John O. Hallquist of LSTC for his support to this research. The support from the Boeing Company is also gratefully acknowledged.

References

- [1] Babuška I. The finite element method for elliptic equations with discontinuous coefficients. *Computing* 1970;5:207–13.
- [2] Srinivasan KR, Matouš K, Geubelle PH. Generalized finite element method for modeling nearly incompressible biomaterial hyperelastic solids. *Comput Meth Appl Mech Eng* 2008;197:4882–93.
- [3] Wu CT, Koishi M. A meshfree procedure for the microscopic analysis of particle-reinforced rubber compounds. *Interact Multiscale Mech* 2009;2:147–69.
- [4] Düster A, Parvizian J, Yang Z, Rank E. The finite cell method for three-dimensional problems for solid mechanics. *Comput Meth Appl Mech Eng* 2008;197:3768–82.
- [5] Yang KH, King AL. A limited review of finite element models developed for brain injury biomechanics research. *Int J Veh Des* 2003;32:116–29.
- [6] Bernardi C, Maday Y, Patera A. Domain decomposition by the mortar element method. In: Kaper HG, Garbey M, editors. *Asymptotic and numerical methods for partial differential equations with critical parameters*. New York: Springer; 1993. p. 269–86.
- [7] Babuška I. The finite element method with Lagrangian multipliers. *Numer Math* 1973;20:179–92.
- [8] Brezzi F, Fortin M. *Mixed and hybrid finite element methods*. New York: Springer; 1991.
- [9] Hansbo A, Hansbo P. An unfitted finite element method, based on Nitsche's method, for elliptic interface problems. *Comput Meth Appl Mech Eng* 2002;191:5537–52.
- [10] Stenberg R. On some techniques for approximating boundary conditions in the finite element method. *J Comput Appl Math* 1995;63:139–48.
- [11] Barbosa HJC, Hughes TJR. The finite element method with Lagrangian multipliers on the boundary: circumventing the Babuška–Brezzi condition. *Comput Meth Appl Mech Eng* 1991;85:109–28.
- [12] Hansbo P. Nitsche's method for interface problems in computational mechanics. *GAMM-Mitt* 2005;282:183–206.
- [13] Babuška I, Caloz G, Osborn J. Special finite element methods for a class of second order elliptic problems with rough coefficients. *SIAM J Numer Anal* 1994;31:945–81.
- [14] Babuška I, Melenk JM. The partition of unity finite element method: basic theory and applications. *Comput Meth Appl Mech Eng* 1996;4:289–314.
- [15] Stroubolis T, Copps K, Babuška I. The generalized finite element method. *Comput Meth Appl Mech Eng* 2001;190:4081–193.
- [16] Babuška I, Banerjee U, Osborn J. Generalized finite element methods – main ideas, results and perspective. *Int J Comput Meth* 2004;1:67–103.
- [17] Duarte CA, Babuška I, Oden JT. Generalized finite element methods for three-dimensional structural mechanics problems. *Comput Struct* 2000;77:215–32.
- [18] Belytschko T, Black T. Elastic crack growth in finite elements with minimal remeshing. *Int J Numer Meth Eng* 1999;45:610–20.
- [19] Sanders JD, Dolbow J, Laursen TA. On methods for stabilizing constraints over enriched interfaces in elasticity. *Int J Numer Meth Eng* 2009;78:1009–36.
- [20] Jean A, Willot F, Cantournet S, Forest S, Jeulin D. Large-scale computations of effective elastic properties of rubber with carbon back fillers. *Int J Multiscale Comput Eng* 2011;9:271–303.
- [21] Parvizian J, Düster A, Rank E. Finite cell method. *Comput Mech* 2007;41:121–33.
- [22] Rüberg T, Cirak F. An immersed finite element method with integral equation correction. *Int J Numer Meth Eng* 2011;86:93–114.
- [23] Li Z. The immersed interface method using a finite element formulation. *Appl Numer Math* 1998;27:253–67.
- [24] Li Z, Yang X. An immersed finite element method for elasticity equations with interfaces. *AMS Contemp Math* 2005;383:285–98.
- [25] Li Z, Lin T, Wu X. New Cartesian grid methods for interface problems using the finite element formulation. *Numer Math* 2003;96:61–98.
- [26] Batra RC, Porfiri M, Spinello D. Treatment of material discontinuity in two meshless local Petrov–Galerkin (MLPG) formulations of axisymmetric heat conduction. *Int J Numer Meth Eng* 2004;61:2461–79.
- [27] Masuda S, Noguchi H. Analysis of structure with material interface by meshfree method. *CMES: Comput Model Eng Sci* 2006;11:131–43.
- [28] Tain R, Ro AC, Liu WK. Conforming local meshfree method. *Int J Numer Meth Eng* 2011;22:335–57.
- [29] Cordes LW, Moran B. Treatment of material discontinuity in the Element-free Galerkin method. *Comput Meth Appl Mech Eng* 1996;139:75–89.
- [30] Krongauz Y, Belytschko T. EFG approximation with discontinuous derivative. *Int J Numer Meth Eng* 1998;41:1215–33.
- [31] Lu H, Kim DW, Liu WK. Treatment of discontinuity in the reproducing kernel element method. *Int J Numer Meth Eng* 2005;63:241–53.
- [32] Rabczuk T, Gracie R, Song JH, Belytschko T. Immersed particle method for fluid-structure interaction. *Int J Numer Meth Eng* 2010;81:48–71.
- [33] Wang D, Chen JS, Sun L. Homogenization of magnetostrictive particle-filled elastomers using an interface-enriched reproducing kernel particle method. *Finite Elem Anal Des* 2003;39:765–82.
- [34] Wang D, Sun Y, Li L. A discontinuous Galerkin meshfree modeling of material interface. *CMES: Comput Model Eng Sci* 2009;45:57–82.
- [35] Wu CT, Park CK, Chen JS. A generalized meshfree approximation for the meshfree analysis of solids. *Int J Numer Meth Eng* 2011;85:693–722.
- [36] Belytschko T, Lu YY, Gu L. Element-free Galerkin methods. *Int J Numer Meth Eng* 1994;37:229–56.
- [37] Liu WK, Jun S, Zhang YF. Reproducing kernel particle methods. *Int J Numer Meth Eng* 1995;20:1081–106.
- [38] Park CK, Wu CT, Kan CD. On the analysis of dispersion property and stable stime step in meshfree method using the generalized meshfree approximation. *Finite Elem Anal Des* 2011;47:683–97.
- [39] Sukumar N. Construction of polygonal interpolants: a maximum entropy approach. *Int J Numer Meth Eng* 2004;61:2159–81.
- [40] Arroyo M, Ortiz M. Local maximum-entropy approximation schemes: a seamless bridge between finite elements and meshfree methods. *Int J Numer Meth Eng* 2006;65:2167–202.
- [41] Shannon CE. A mathematical theory of communication. *Bell Syst Tech J* 1961;27:547–61.
- [42] Jaynes ET. Information theory and statistical mechanics. *Phys Rev* 1957;106:620–30.
- [43] Ortiz A, Puso MA, Skumar N. Maximum-entropy meshfree method for compressible and near-incompressible elasticity. *Comput Meth Appl Mech Eng* 2010;199:1859–71.

- [44] Millan D, Rosolen A, Arroyo M. Thin shell analysis from scattered points with maximum-entropy approximation. *Int J Numer Meth Eng* 2011;85:723–51.
- [45] Wu CT, Hu W. Meshfree-enriched simplex elements with strain smoothing for the finite element analysis of compressible and near-incompressible solids. *Comput Meth Appl Mech Eng* 2011;200:2991–3010.
- [46] Wu CT, Koishi M. Three-dimensional meshfree-enriched finite element formulation for micromechanical hyperelastic modeling of particulate rubber composites. *Int J Numer Meth Eng* 2012. doi:<http://dx.doi.org/10.1002/nme.4306>.
- [47] Brenner SC, Scott LR. The mathematical theory of finite element methods. New York: Springer; 1999.
- [48] Chen JS, Pan C, Wu CT, Liu WK. Reproducing kernel particle methods for large deformation analysis of non-linear structures. *Comput Meth Appl Mech Eng* 1996;139:195–227.
- [49] Chen JS, Wu CT, Belytschko T. Regularization of material instabilities by meshfree approximations with intrinsic length scales. *Int J Numer Meth Eng* 2000;47:1303–22.
- [50] Chen JS, Wang HP. New boundary condition treatments in meshfree computation of contact problems. *Comput Meth Appl Mech Eng* 2000;187:441–68.
- [51] Wang HP, Wang D. Efficient meshfree computation with fast treatment of essential boundary conditions for industrial applications. *J Eng Mech ASCE* 2009;135:1147–54.
- [52] Han W, Meng X. Error analysis for the reproducing kernel particle method. *Comput Meth Appl Mech Eng* 2001;190:6157–81.
- [53] About L, Maire E, Buffière JY, Fougères R. Characterization by X-ray computed tomography of decohesion, porosity growth and coalescence in model metal matrix composites. *Acta Mater* 2001;49:2055–63.
- [54] Chawla N, Sidhu RS, Ganesh VV. Three-dimensional visualization and microstructure-based modeling of deformation in particle-reinforced composites. *Acta Mater* 2006;54:1541–8.
- [55] Madi K, Forest S, Boussuge M, Gailliègue S, Iataste E, Buffière JY, et al. Finite element simulations of the deformation of fused-cast refractories based on X-Ray computed tomography. *Comput Mater Sci* 2007;39:224–9.
- [56] Mourad HM, Dolbow J, Harari I. A bubble-stabilized finite element method for Dirichlet constraints on embedded interfaces. *Int J Numer Meth Eng* 2006;69:1–21.
- [57] Timoshenko SP, Goodier JN. Theory of elasticity. New York: McGraw-Hill; 1970.